

# Upper-mantle anisotropy in the southeastern margin of Tibetan Plateau revealed by fullwave SKS splitting intensity tomography

Yi Lin<sup>1,2</sup> and Li Zhao<sup>1,3</sup>

<sup>1</sup>School of Earth and Space Sciences, Peking University

<sup>2</sup>Ministry of Education, Key Laboratory of Earth Exploration and Information Techniques, Chengdu University of Technology

<sup>3</sup>Hebei Hongshan National Geophysical Observatory, Peking University

March 05, 2024

## Abstract

The southeastern margin of the Tibetan Plateau has undergone complex deformation since the Cenozoic, resulting in a high level of seismicity and seismic hazard. Knowledge about the seismic anisotropy provides important insight about the deformation mechanism and the regional seismotectonics beneath this tectonically active region. In this study, we conduct fullwave multi-scale tomography to investigate the seismic anisotropy in the southeastern margin of the Tibetan Plateau. Broadband records at 111 permanent stations in the region from 470 teleseismic events are used to obtain 5,216 high-quality SKS splitting intensity measurements, which are then inverted in conjunction with 3D sensitivity kernels to obtain an anisotropic model with multi-scale resolution. Resolution tests show that our dataset recovers anisotropy anomalies reasonably well on the scale of  $1^{\circ} \times 1^{\circ}$  horizontally and  $\sim 100$  km vertically. Our result suggests that in the southeastern margin of the Tibetan Plateau the deformation in the lithosphere and asthenosphere are decoupled. The anisotropy in the lithosphere varies both laterally and vertically as a result of dynamic interactions of neighboring blocks as well as lithospheric reactivation. The anisotropy in the asthenosphere largely follows the direction of regional absolute plate motion. The SKS splittings observed at the surface are shown to be consistent with the vertical integral of our depth-dependent anisotropy model over lithospheric and asthenospheric depths.

1

2

3 **Upper-mantle anisotropy in the southeastern margin of Tibetan Plateau revealed by fullwave SKS splitting**

4 **intensity tomography**

5 Yi Lin<sup>1,2</sup>, Li Zhao<sup>1,3</sup>

6 <sup>1</sup> School of Earth and Space Sciences, Peking University, Beijing 100871, China.

7 <sup>2</sup> Key Laboratory of Earth Exploration and Information Techniques of the China Ministry of Education,  
8 Chengdu University of Technology, Chengdu 610059, China.

9 <sup>3</sup> Hebei Hongshan National Geophysical Observatory, Peking University, Beijing 100871, China.

10

11

12 Corresponding author: L. Zhao (lizhaopku@pku.edu.cn)

13

14

15 **Key Points:**

- 16 • A 3D shear-wave anisotropy model for the SE margin of the Tibetan Plateau is obtained by  
17 fullwave SKS splitting intensity tomography
- 18 • Result shows a decoupling of lithosphere and asthenosphere deformations in the region, but a  
19 coupling under Tibetan Plateau
- 20 • Lithospheric anisotropy has a complex pattern, whereas asthenospheric anisotropy follows the  
21 APM

22

## 23 **Abstract**

24 The southeastern margin of the Tibetan Plateau has undergone complex deformation since the Cenozoic,  
25 resulting in a high level of seismicity and seismic hazard. Knowledge about the seismic anisotropy provides  
26 important insight about the deformation mechanism and the regional seismotectonics beneath this tectonically  
27 active region. In this study, we conduct fullwave multi-scale tomography to investigate the seismic  
28 anisotropy in the southeastern margin of the Tibetan Plateau. Broadband records at 111 permanent stations  
29 in the region from 470 teleseismic events are used to obtain 5,216 high-quality SKS splitting intensity  
30 measurements, which are then inverted in conjunction with 3D sensitivity kernels to obtain an anisotropic  
31 model with multi-scale resolution. Resolution tests show that our dataset recovers anisotropy anomalies  
32 reasonably well on the scale of  $1^\circ \times 1^\circ$  horizontally and  $\sim 100$  km vertically. Our result suggests that in the  
33 southeastern margin of the Tibetan Plateau the deformation in the lithosphere and asthenosphere are decoupled.  
34 The anisotropy in the lithosphere varies both laterally and vertically as a result of dynamic interactions of  
35 neighboring blocks as well as lithospheric reactivation. The anisotropy in the asthenosphere largely follows the  
36 direction of regional absolute plate motion. The SKS splittings observed at the surface are shown to be  
37 consistent with the vertical integral of our depth-dependent anisotropy model over lithospheric and  
38 asthenospheric depths.

39 **Keywords:** seismic anisotropy; splitting intensity; finite-frequency; fullwave tomography; southeastern  
40 Tibetan Plateau

41

## 42 **Plain Language Summary**

43 The southeastern margin of the Tibetan Plateau has undergone significant deformation since the Cenozoic  
44 due to the collision between the Eurasian and Indian plates in the south and interactions with the Yangtze  
45 Craton in the east. Knowledge about the upper mantle seismic anisotropy helps us understand the

46 deformation and dynamic evolution. In this study, we conduct fullwave multi-scale anisotropy  
47 tomography for the southeastern margin of the Tibetan Plateau using 5,216 high-quality SKS splitting  
48 intensity measurements obtained from the broadband records of 470 teleseismic events at 111 stations. Our  
49 result shows a decoupling between the lithosphere and asthenosphere deformations in the southeastern margin  
50 of the Tibetan Plateau. The anisotropy in the lithosphere varies both laterally and vertically as a result of the  
51 dynamic interactions of neighboring blocks as well as lithospheric reactivation. The anisotropy in the  
52 asthenosphere is largely parallel to the regional absolute plate motion, and the SKS splitting observed at the  
53 surface is the result of vertical integration of the anisotropy effect through the lithosphere and asthenosphere.

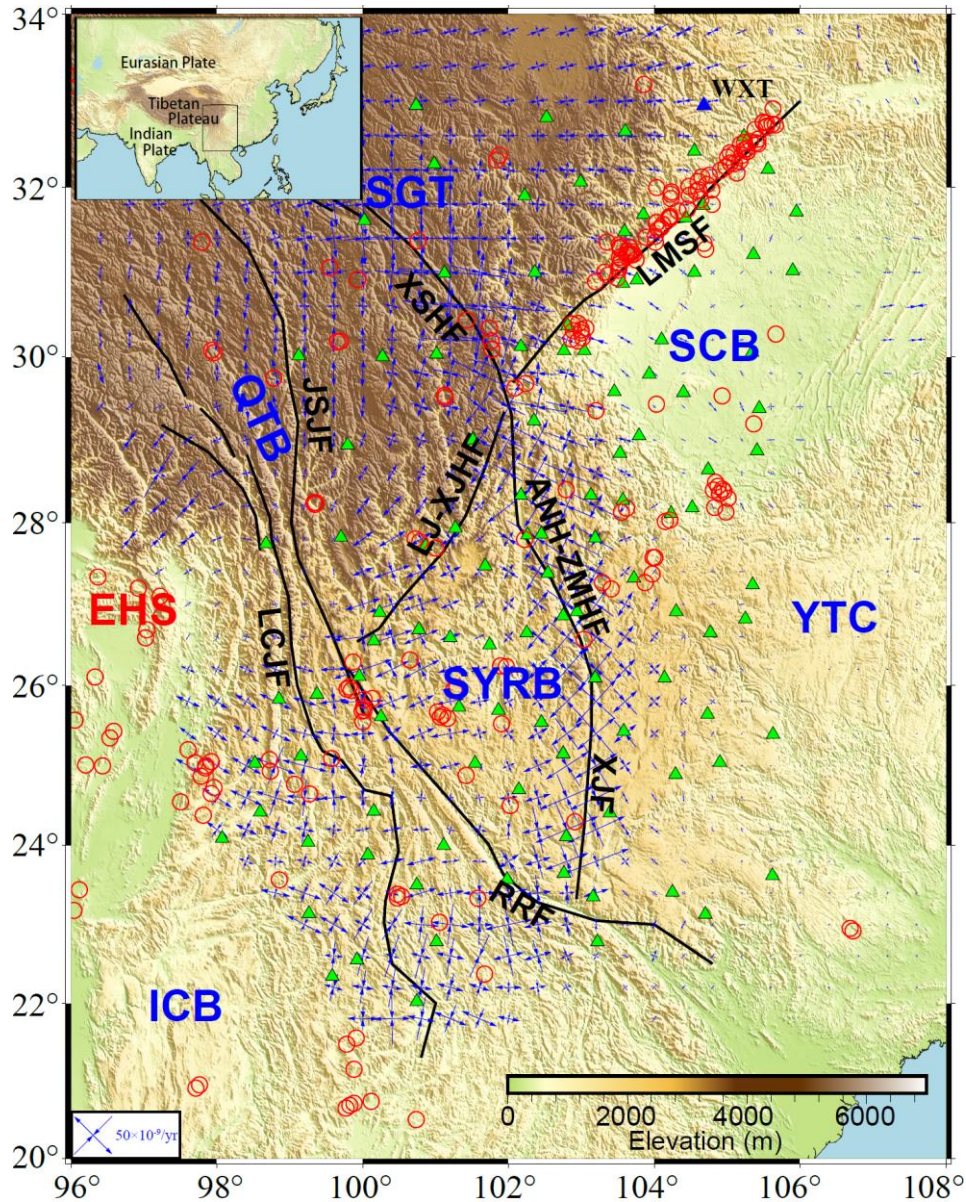
54

## 55 **1 Introduction**

56 The ongoing Indian-Eurasian continental collision has resulted in the largest plateau on Earth and caused  
57 widespread deformation in central and east Asia (Yin & Harrison, 2000; Kind et al., 2002). Despite  
58 numerous efforts, questions remain about the dynamics of the lithospheric deformation and asthenosphere  
59 flow beneath the Tibetan Plateau and the surrounding regions (Royden et al., 2008).

60 The southeastern (SE) margin of the Tibetan Plateau involves many active tectonic blocks (Figure 1),  
61 including the Songpan-Ganzi Terrane (SGT), the Sichuan Basin (SCB), the Sichuan-Yunnan Rhombic  
62 Block (SYRB), the Indo-China Block (ICB), the Qiangtang Block (QTB), and the Yangtze Craton (YTC).  
63 The SGT is part of central Tibetan Plateau. Its eastern part is separated from the SCB and SYRB by the  
64 Longmenshan Fault (LMSF) and Lijiang-Xiaojinhe Fault (LJ-XJHF), respectively, and bounded in the south  
65 by the Jinshajiang Fault (JSJF) from the QTB. The convergence between the Indian and Eurasian plates  
66 caused the SGT to expand eastward against the SCB during the Cenozoic (Yin & Harrison, 2000). GPS  
67 observations show eastward crustal motion of the eastern SGT with the crustal strain rate decreasing  
68 abruptly from ~20 mm/year (relative to the YTC reference frame) in the interior SGT to ~3–4 mm/year or  
69 less in the vicinity of central and southern segments of the LMSF, indicating that the eastward expansion  
70 of the SGT is apparently resisted by the SCB (Shen et al., 2005; Zhang, 2013) In addition, there is also an  
71 apparent clockwise rotation of the GPS velocities around the Eastern Himalaya Syntax (EHS). Low-  
72 velocity and high-conductivity anomalies in the mid-lower crust under the SGT revealed by geophysical  
73 studies (Zhao et al., 2012; Bao et al., 2020) suggest the existence of mid-lower crustal flow. However,  
74 these geophysical anomalies show strong lateral heterogeneity in eastern Tibet, implying a complex  
75 process of deformation in the region. The SCB and SYRB are both parts of the YTC (Zhang et al., 2013;  
76 Li et al., 2021). The former forms the rigid and stable northwestern margin of the YTC, while the crust of  
77 the latter is extruding southeastward along the Anninghe-Zemuhe Fault (ANH-ZMHF) and Xiaojiang Fault

78 (XJF) in the east and the Red River Fault (RRF) in the southwest (Zhang et al., 2003). The Lancangjiang  
 79 Fault (LCJF) separates the narrow QTJB in the east and the ICB in the west. Crustal movements are  
 80 predominantly characterized by a clockwise rotation around the Eastern Himalayan Syntaxis (EHS),  
 81 transforming the movement of the plateau material from eastward north of the syntaxis to southeastward  
 82 and southward further south (Wang & Shen, 2020).



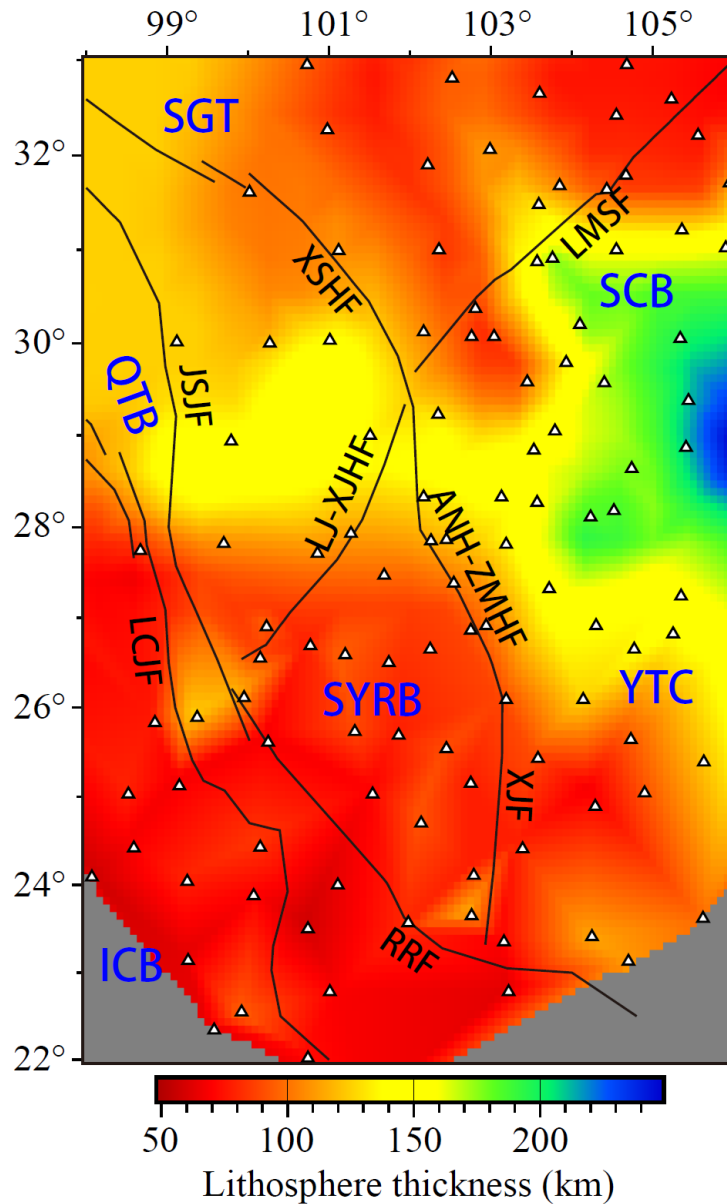
83

84 **Figure 1.** Map of the tectonic environment of SE margin of Tibetan Plateau with seismic stations (green-  
 85 filled triangles) and epicenters (red open circles) of earthquakes of magnitude 5 and above from 2000 to

86 2022. The blue triangle marks the station WXT for which SKS waveforms, splitting intensities and  
87 sensitivity kernels are shown in Figures 4, 5 and 7, respectively. Major active faults are shown by thick  
88 black lines with abbreviated names in black, including LMSF: Longmenshan Fault; XSHF: Xianshuihe  
89 Fault; JSJF: Jinshajiang Fault; LCJF: Lancangjiang Fault; LJ-XJHF: Lijiang-Xiaojinhe Fault; ANH-  
90 ZMHF: Anninghe-Zemuhe Fault; XJF: Xiaojiang Fault; and RRF: Red River Fault. Major active tectonic  
91 blocks are indicated by abbreviated texts in blue, including SGT: Songpan-Ganzi Terrane; SCB: Sichuan  
92 Basin; QTB: Qiangtang Block; SYRB: Sichuan-Yunnan Rhombic Block; YTC: Yangtze Craton; and ICB:  
93 Indo-China Block. EHS stands for the Eastern Himalaya Syntax. Blue cross arrows show the surface strain  
94 rate derived from GPS observation (Wang & Shen, 2020). Background color shows the topography. The  
95 black box in the inset map indicates the location of the main figure.

96 Over the past two decades, a large number of seismic stations have been deployed in the SE margin  
97 of the Tibetan Plateau. Waveforms recorded by the growing number of broadband stations have provided  
98 crucial data for studying the structure and dynamics of the crust and upper mantle beneath the region, such  
99 as variation in crustal thickness (Wang et al., 2017; Xu et al., 2020), widespread low-velocity anomalies in  
100 mid-lower crust revealed by receiver function analysis (Hu et al., 2005; Xu et al., 2007; Zhang et al., 2009;  
101 Wang et al., 2010), Lg-wave high-attenuation zones (Zhao et al., 2013; Wei & Zhao, 2019), joint inversion  
102 of receiver function and surface wave dispersion (Liu et al., 2014), and body- and surface-wave  
103 tomographies (Huang et al., 2002; Wang et al., 2003; Huang et al., 2009; Li et al., 2009; Yang et al., 2019;  
104 Wei & Zhao, 2022).

105 Across the LMSF, the drastic change in elevation from ~5–6 km in the west to a few hundred meters  
106 in the east suggests significant variations in the lithospheric thickness, as illustrated in Figure 2, where the  
107 global model LITHO1.0 (Pasyanos et al., 2014) is shown north of 27°N. South of 27°N, LITHO1.0 is  
108 rather uniform, and the regional model of Yang et al. (2017) is depicted. In this region, the lithosphere has  
109 a thickness of less than 100 km in the northern and southern parts but ~150 km at the mid latitudes. The  
110 thickest lithosphere is more than 200 km beneath the SCB.



111

112 **Figure 2.** Lithosphere thickness map. The global model LITHO1.0 (Pasyanos et al., 2014) is shown for  
 113 the region north of 27°N, whereas to the south the regional model of Yang et al. (2017) is depicted. Names  
 114 of major faults and tectonic blocks are the same as in Figure 1.

115 Seismic anisotropy in the upper mantle is an important proxy for deformation. There have been  
 116 numerous studies devoted to crustal anisotropy beneath the SE Tibetan Plateau utilizing different methods,  
 117 such as Pms splitting (Sun et al., 2012; Cai et al., 2016; Han et al., 2020), anisotropic tomography of P  
 118 and Pn waves (Lei et al., 2014; Huang et al., 2018), surface wave anisotropic tomography (Yang et al.,

119 2010; Yao et al., 2010; Legendre et al., 2015; Zhang et al., 2023), and the splitting of shear waves (Shi et al.,  
120 2012). In the upper crust, the fast axis directions are mainly parallel to the strike of active faults (e.g., Yao  
121 et al., 2010; Shi et al., 2012; Huang et al., 2018), whereas the anisotropic pattern in the lower crust is  
122 different. Huang et al. (2018) showed that the fast velocity direction deviates from the strikes of active faults  
123 significantly using P-wave anisotropic tomography. Han et al. (2020) used Markov-chain Monte Carlo  
124 inversion of receiver functions to isolate the effect of potential dipping interfaces. Their results showed  
125 that the fast axis directions in the lower crust are in good agreement with topography, implying that the  
126 gravitational potential may be the driving force for the crustal deformation in southeastern Tibet.

127 XKS-wave splitting is routinely used to investigate the anisotropic structure in the upper mantle (Long  
128 & Becker, 2010). Flesch et al. (2005) jointly analyzed GPS, surface geology and shear-wave splitting  
129 measurements and argued for vertically coherent deformation in the crust and upper mantle in the Tibetan  
130 Plateau but a decoupling in Yunnan Province in southwestern China. Lev et al. (2006) also suggested a  
131 lithosphere-asthenosphere decoupling in Yunnan using shear-wave splitting observations, but they were not  
132 able to determine the degree of coupling beneath the Tibetan Plateau. Based on a joint analysis of a larger  
133 dataset of shear-wave splitting measurements and GPS observations, Wang et al. (2008) argued for crust-  
134 mantle coupling in the Tibetan Plateau and the surrounding regions.

135 Substantial efforts have been made to develop a theoretical framework as well as practical strategies  
136 for inversion for the 3D distribution of anisotropy. A fullwave approach has been developed for the  
137 measurement of shear-wave splitting intensities and interpretation in terms of shear-wave azimuthal anisotropy  
138 parameters (Chevrot, 2000; Favier & Chevrot, 2003; Chevrot, 2006; Sieminski et al., 2008; Monteiller &  
139 Chevrot, 2011; Lin et al., 2014a), which has been applied to anisotropy tomographies for southern  
140 California (Monteiller & Chevrot, 2011; Lin et al., 2014b), the High Lava Plain (Mondal & Long, 2020),  
141 and the southeastern Tibetan Plateau (Huang & Chevrot, 2021). The depth variations of anisotropy obtained

142 by these studies have shed new lights in understanding the sources of anisotropy and the associated mantle  
143 dynamics.

144 In this study, we conduct a fullwave multiscale anisotropy tomography for the SE margin of Tibetan  
145 Plateau. We collect seismic records at regional permanent broadband stations from globally distributed  
146 earthquakes and obtain high-quality measurements of SKS splitting intensities. We then invert the  
147 splitting intensities using a wavelet-based parameterization of the 3D model to achieve a multi-scale  
148 resolution of the anisotropic structure. We also provide an interpretation of our anisotropic model for  
149 the SE margin of Tibetan Plateau in terms of regional geodynamics.

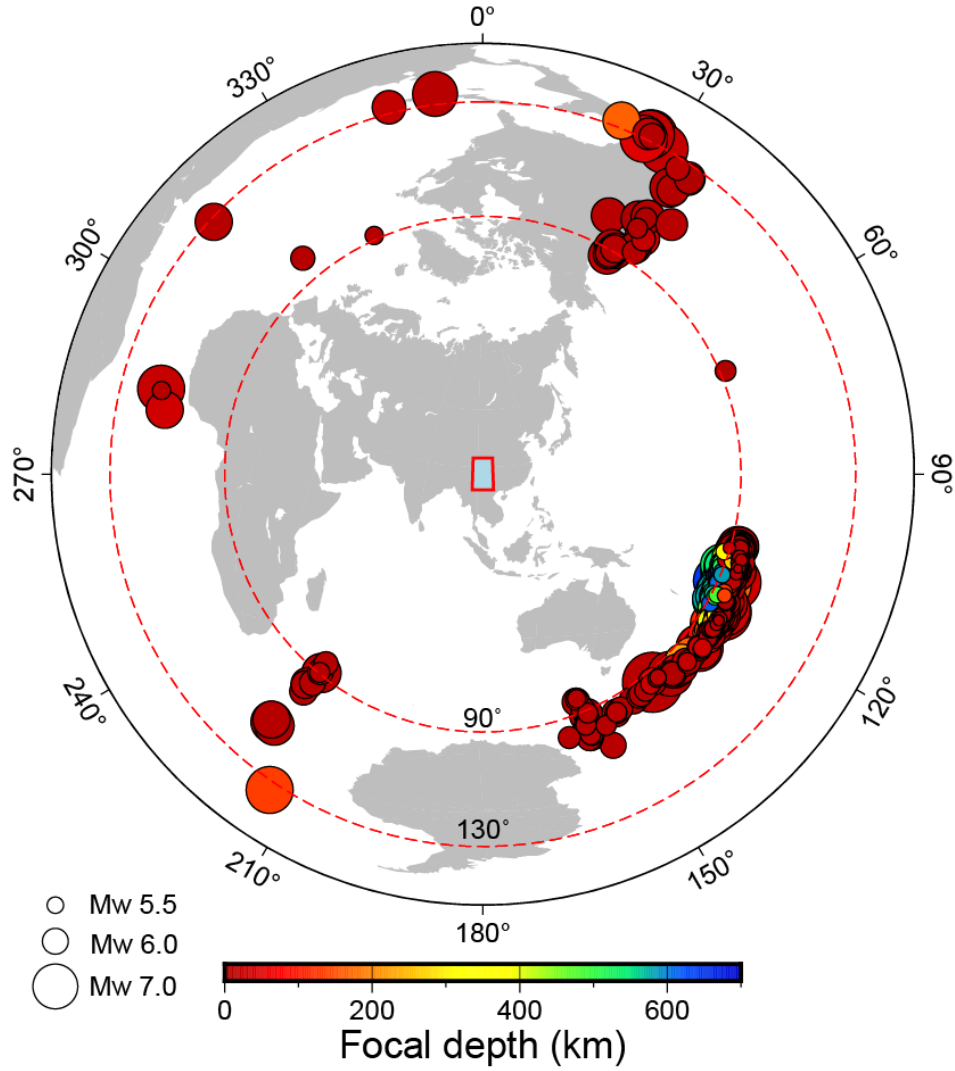
## 150 **2 Data and Methods**

### 151 **2.1 Waveform records**

152 We collect waveforms recorded by 111 permanent broadband stations (green triangles in Figure 1)  
153 deployed in the study region. To guarantee a wide range of azimuthal distribution, we select events of  
154 magnitude  $M_w \geq 5.5$  from 2009 to 2020, located in the epicentral distance range of  $90^\circ$ – $130^\circ$ . After quality  
155 control of the waveforms and removal of outliers of the data (see Section 2.2), a total of 470 events are  
156 used in the subsequent inversions. Figure 3 displays the event distribution.

### 157 **2.2 Splitting intensity measurements**

158 Shear-wave splitting measurement is nowadays a routine procedure in the study of seismic anisotropy.  
159 Several previous studies have documented the measured SKS splitting parameters (fast directions and delay  
160 times) at stations in our study region (e.g., Chang et al., 2015; Yang et al., 2018; Liu et al., 2020; Huang  
161 & Chevrot, 2021; Li et al., 2021). In this study, we invert for the 3D anisotropy structure using the  
162 splitting intensity (SI) measurements obtained by computing the zero-lag cross-correlation between the  
163 transverse-component record and the time derivative of the radial-component record (Chevrot, 2000).



164

165 **Figure 3.** Distribution of 470 teleseismic events used for SKS splitting intensity inversion in this study.  
 166 Events of magnitudes Mw5.5 and greater in the epicentral distance range of 90°–130° during 2009–2020  
 167 are selected. The red box in the center indicates the study area.

168

For a given station, the SI of the SKS wave from the  $i$ -th event is defined as

169

$$S_i = -2 \frac{\int_{t_{i1}}^{t_{i2}} \dot{u}_i^R(t) u_i^T(t) dt}{\int_{t_{i1}}^{t_{i2}} [\dot{u}_i^R(t)]^2 dt}, \quad (1)$$

170

where  $[t_{i1}, t_{i2}]$  is the time window for the SKS wave, and  $u_i^R(t)$  and  $u_i^T(t)$  are the radial and transverse-

171

component records, respectively, from the  $i$ -th event. A dot above a variable indicates derivative with

172

respect to time. The conventional SKS splitting parameters at the given station, namely the fast-direction

173 azimuth  $\theta$  and delay time  $\Delta t$ , are related to the SIs measured at the station from all events through a  
 174 sinusoidal curve fitting (Chevrot, 2000; Lin et al., 2014a):

$$175 \quad S_i = \Delta t \sin 2(\theta - \theta_i^b), \quad (2)$$

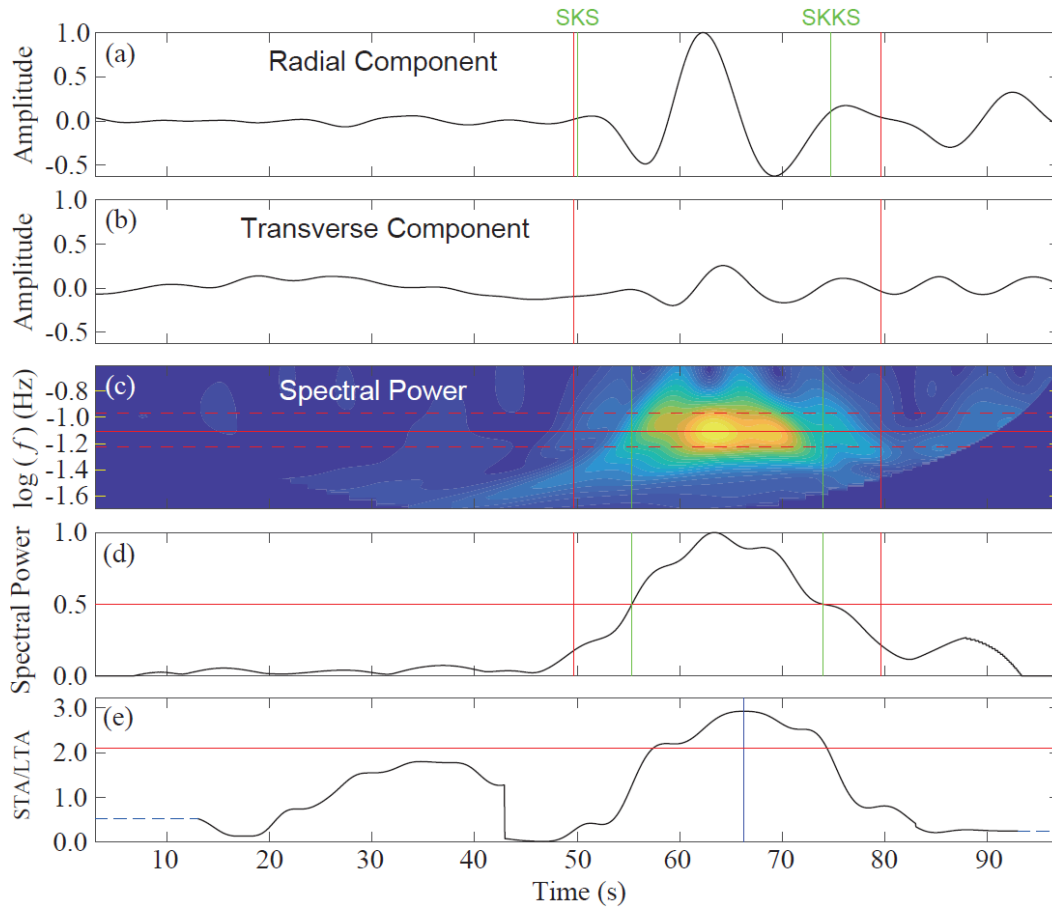
176 where  $\theta_i^b$  is the back azimuth of the  $i$ -th event.

177 In this study, we obtain the SI measurements of SKS waves with the help of SplitRacer (Link et al.,  
 178 2022), an efficient and automatic toolbox developed for the measurement and quality control of XKS  
 179 splittings. An example of SplitRacer processing is shown in Figure 4. We use SplitRacer to determine the  
 180 SKS time window automatically, followed by a manual check on the quality of the SKS signals. Then, we  
 181 calculate the SIs using Eq. (1). The period band we use in this study is 8–50 s considering the dominant  
 182 periods of the SKS signals as well as minimizing the interference with neighboring phases. As shown in  
 183 Figure 4, the spectral powers of the radial- and transverse-component records are calculated by the short-  
 184 time Fourier transform (Quatieri, 2006) and summed. Then, the dominant frequency band of the SKS  
 185 waveform can be identified (between the red dashed horizontal lines in Figure 4c). At each time, the  
 186 powers within the dominant frequency band are summed (Figure 4d), which defines the SKS window by  
 187 the two crossing points at 50% of the peak level (vertical green lines in Figure 4d). The final SKS window  
 188 is given by either expanding or shrinking the 50% energy window to a fixed 30-s window (red vertical  
 189 lines). After completing the quality check using SplitRacer, we obtain a total of 12,457 SKS wave SI  
 190 measurements.

191 Following Chevrot (2000), we estimate the uncertainty of each SI measurement using the following  
 192 equation

$$193 \quad \sigma_i = \sqrt{\frac{1}{N_i} \left\{ \sum_{j=1}^{N_i} [u_i^T(t_j)]^2 - \frac{S_i^2}{4} \sum_{j=1}^{N_i} [\dot{u}_i^R(t_j)]^2 \right\}}, \quad (3)$$

194 where  $S_i$  is the  $i$ -th SI measurement, and  $N_i$  is the number of time samples used for the window to obtain  
 195 the measurement.



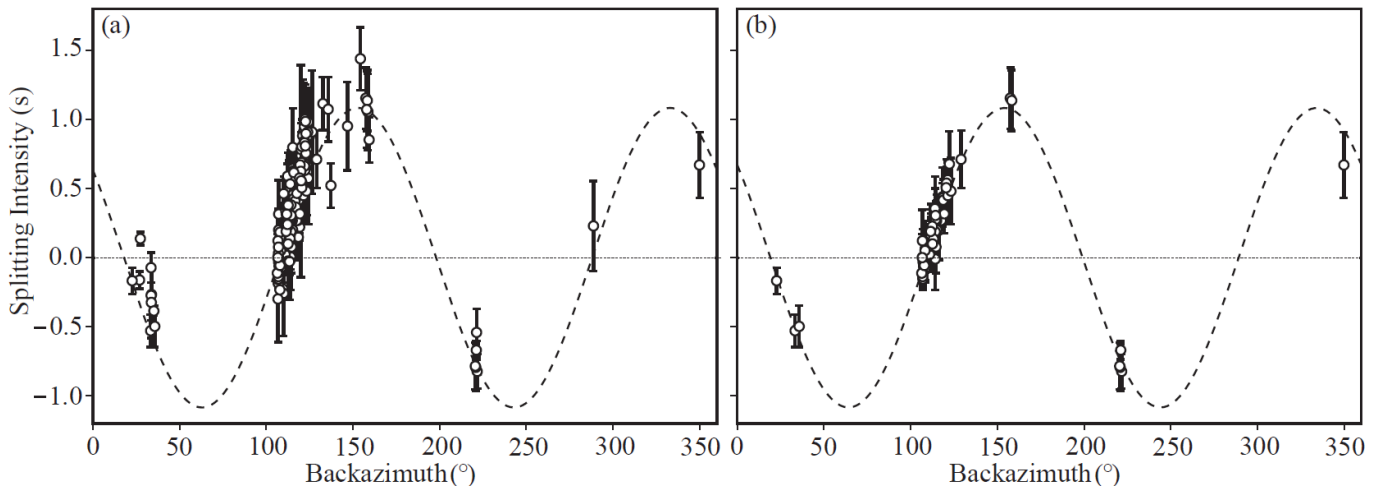
196

197 **Figure 4.** An example of SKS window selection using SplitRacer. (a) and (b) show normalized radial and  
 198 transverse records, respectively, around the SKS arrival at station WXT (blue triangle in Figure 1) from  
 199 the 24 June 2019 earthquake in New Zealand with a back azimuth of  $122^\circ$ . The green lines mark the  
 200 theoretical SKS and SKKS arrival times corresponding to the event of interest. Red vertical lines mark  
 201 the start and end times of the final window used for SI measurement. (c) Summed spectral power of the  
 202 spectrogram of the radial and transverse records in (a) and (b). The red horizontal line marks the frequency  
 203 of maximum spectral power, and the red dashed lines show the frequency bounds of more than 80% of  
 204 the maximum. The green vertical lines mark the time window in which the summed spectral power is  
 205 more than 50% of the maximum. (d) Summed spectral power over all frequencies. The green vertical lines  
 206 mark the time window in which the summed spectral energy is more than 50% of the maximum. (e)  
 207 STA/LTA ratio of the radial-component record used as quality check. The blue vertical line denotes the  
 208 time when the STA/LTA ratio reaches its peak within the window determined in (d). The red horizontal  
 209 line is the acceptance threshold of 2.1 (Link et al., 2022).

210

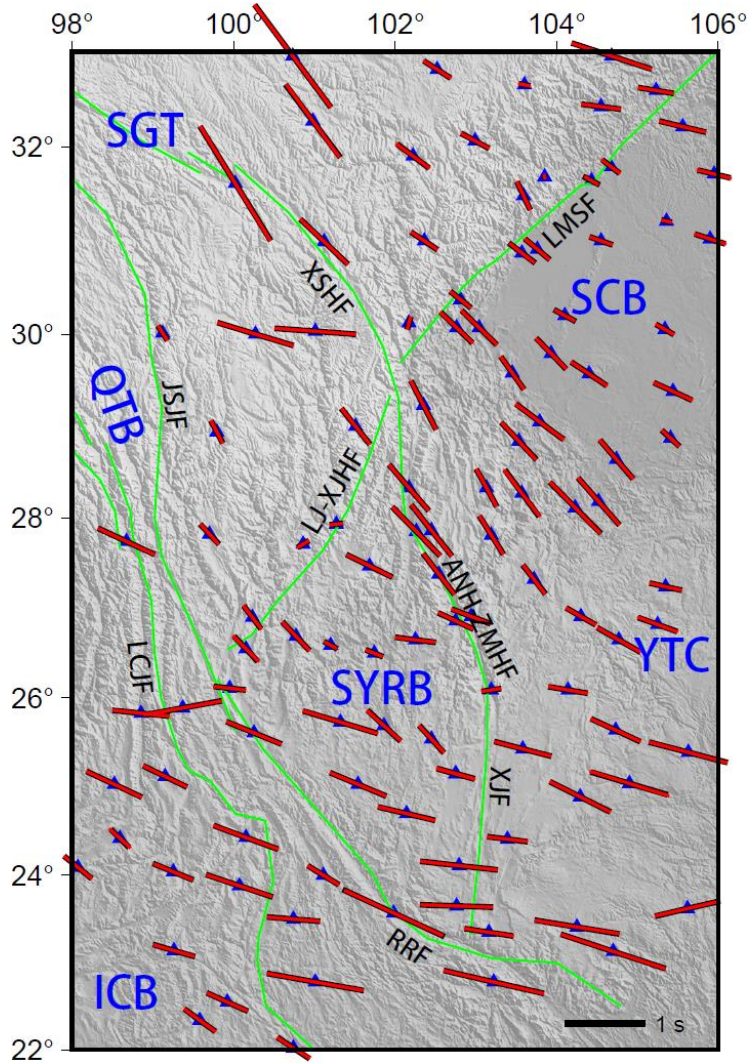
We further clean our dataset of outliers based on two criteria: (1) At a given station, SI measurements

211 with uncertainties  $\sigma_i$  larger than 1.5 times the average uncertainty  $\bar{\sigma}$  for that station, i.e.  $\sigma_i > 1.5\bar{\sigma}$ , are  
 212 removed; (2) all SI measurements at a given station are fit by a sinusoidal curve, and measurements that  
 213 deviate from the sinusoidal curves by more than  $2\sigma_i$  are also removed. After removing the outliers, we  
 214 retain a total of 5,216 high-quality SI measurements as our final dataset for subsequent anisotropy  
 215 inversion. The standard deviation of the final dataset (the average of uncertainties of all retained data) is  
 216 0.074 s. Figure 5 shows the effect on the distribution of SI measurements before and after applying the  
 217 above two criteria for station WXT, which reduces the number of SI data from 184 to 61.



218 **Figure 5.** Variations of measured SI with event back azimuth for station WXT (blue triangle in Figure 1)  
 219 before (a) and after (b) removal of SI outliers. The vertical error bars show two standard deviations ( $2\sigma_i$ )  
 220 of individual measurements. The dashed lines represent the sinusoidal curves that best fit the  
 221 measurements. According to Eq. (2), the conventional SKS splitting parameters for this station are:  $\Delta t =$   
 222 1.08 s and  $\theta = 109.14^\circ$ .  
 223

224 Based on Eq. (2), we can obtain the conventional fast-direction azimuth  $\theta$  and delay time  $\Delta t$  at each  
 225 station using all the SI measurements, and they are displayed in Figure 6. The spatial distribution of  $\theta$  has  
 226 a similar pattern as seen in previous studies, i.e. a generally NW-SE oriented fast axis and a nearly uniform  
 227 E-W alignment of the fast-axis directions south of  $\sim 26^\circ\text{N}$  latitude.



228

229 **Figure 6.** Black line segments show the conventional SKS fast-direction azimuths and delay times at all  
 230 station obtained from the SI measurements according to Eq. (2). Red line segments are fast-direction  
 231 azimuths and delay times derived from Eq. (2) based on the model-predicted SIs obtained by integrating  
 232 the sensitivity kernels (see Figure 7) with the anisotropy model in Figure 12 according to Eq. (4). Names  
 233 of major faults and tectonic blocks are the same as in Figure 1.

234

### 2.3 Multiscale inversion for 3D anisotropic structure

235

We implement the full-wave multiscale anisotropy tomography framework developed by Lin et al.  
 236 (2014b). Here we briefly describe our methodology. Interested readers may consult Lin et al. (2014b) for  
 237 a full description of the method.

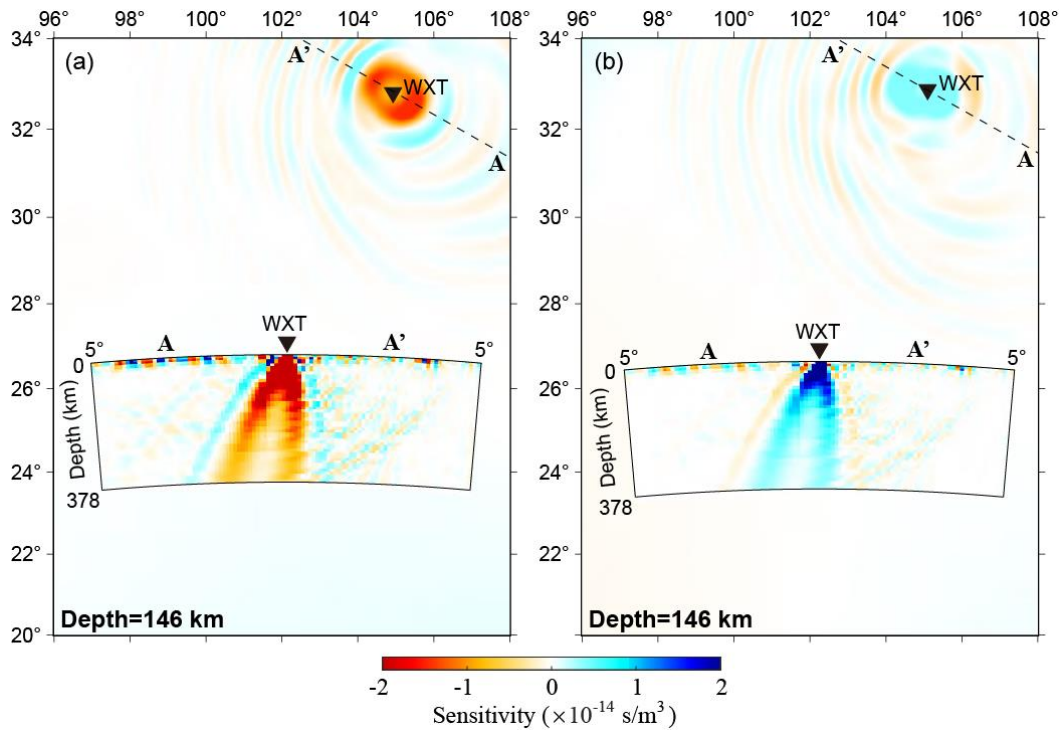
238

Becker et al. (2006) pointed out that the upper-mantle anisotropy is mainly hexagonal with strongly

239 correlated parameters  $\varepsilon$  and  $\gamma$  quantifying the P- and S-wave anisotropy, respectively, and the ellipticity  
 240 parameter  $\delta$ . Furthermore, Zhao & Chevrot (2011) demonstrated that the SI of an SKS wave is mostly  
 241 sensitive to  $\gamma$ , and is about 10 times larger than to the isotropic heterogeneity. This allows us to simplify  
 242 the modeling of upper mantle anisotropy in two aspects: (1) it is sufficient to use a 1D reference model;  
 243 and (2) the anisotropy can be described by only two parameters: the strength of anisotropy  $\gamma$  and the azimuth  
 244  $\phi_f$  of the symmetry axis of anisotropy. We assume that the symmetry axis is horizontal since the sub-  
 245 vertically propagating SKS waves are insensitive to the dip angle of the symmetry axis of anisotropy  
 246 (Mondal & Long, 2019). Note that the anisotropy strength  $\gamma$  and azimuth  $\phi_f$  are spatially varying, and  
 247 the dependence of the SI on  $\phi_f$  is nonlinear. As documented in Favier & Chevrot (2003), we can  
 248 introduce two independent parameters,  $\gamma_c = \gamma \cos(2\phi_f)$  and  $\gamma_s = \gamma \sin(2\phi_f)$ , to enable a linear  
 249 relationship with the SI measurement

$$250 \quad S = \iiint [K_{\gamma_c}^S(\mathbf{r})\gamma_c(\mathbf{r}) + K_{\gamma_s}^S(\mathbf{r})\gamma_s(\mathbf{r})]d\mathbf{r}, \quad (4)$$

251 where  $K_{\gamma_c}^S$  and  $K_{\gamma_s}^S$  are the Fréchet sensitivity kernels of the splitting intensity  $S$  to  $\gamma_c$  and  $\gamma_s$ , respectively.  
 252 After obtaining  $\gamma_c$  and  $\gamma_s$  from a linear inversion, we can obtain the more familiar anisotropy parameters  
 253 by utilizing the relations:  $\phi_f(\mathbf{r}) = 0.5 \tan^{-1}[\gamma_s(\mathbf{r})/\gamma_c(\mathbf{r})]$  and  $\gamma(\mathbf{r}) = \sqrt{[\gamma_c(\mathbf{r})]^2 + [\gamma_s(\mathbf{r})]^2}$ . In this  
 254 study, we use PREM (Dziewonski & Anderson, 1981) as the reference model and compute the sensitivity  
 255 kernels using the normal-mode summation algorithm developed by Zhao & Chevrot (2011). Examples of  
 256 the Fréchet kernels for  $\gamma_c$  and  $\gamma_s$  are shown in Figure 7. Chevrot (2006) first noted the similarity between  
 257 the definitions of SI in Eq. (1) and finite-frequency traveltimes (e.g. Dahlen et al., 2000; Zhao et al., 2000),  
 258 which implies that the sensitivity kernels of SI to anisotropy parameters exhibit the distinct banana-doughnut  
 259 shapes typical in the sensitivities of finite-frequency traveltimes to isotropic velocities, as shown in Figure 7.



260

261 **Figure 7.** Examples of the sensitivity kernels of the SI to shear wave anisotropy parameters  $\gamma_c$  (a) and  $\gamma_s$   
 262 (b) shown in mapviews for the 146-km depth and in profiles (insets) along source-receiver path AA' for  
 263 station WXT (blue triangle in Figure 1). The SKS wave is from the 24 June 2019 event in New Zealand  
 264 with a back azimuth of 122°, and the waveforms are shown in Figure 4.

265 As in Lin et al. (2014b), we adopt a wavelet-based model parameterization (Chiao & Kuo, 2001) to  
 266 obtain multi-scale resolutions in both sparsely- and densely-sampled regions of data coverage. The inverse  
 267 problem can be expressed as:

$$268 \quad (\mathbf{G}\mathbf{W}^{-1})(\mathbf{W}\mathbf{m}) = \mathbf{d}, \quad (5)$$

269 where  $\mathbf{G}$  is the Gram matrix containing the Fréchet kernels,  $\mathbf{W}$  is the 3D wavelet transform matrix,  $\mathbf{m}$  is  
 270 the vector containing the model parameters at spatial nodes, and  $\mathbf{d}$  is the data vector of the SI  
 271 measurements. In this study, we first parameterize the model by a 3D mesh with  $33 \times 33$  nodes horizontally  
 272 and 17 nodes vertically, and apply the operator  $(\mathbf{W}^{-1})^T$  on each row of  $\mathbf{G}$ . A damped least-squares solution  
 273 to the inverse problem in Eq. (5) is solved by the LSQR algorithm (Paige & Saunders, 1982), with the  
 274 damping factor  $\lambda$  selected empirically by a series of inversion experiments (see Section 2.4), and the final

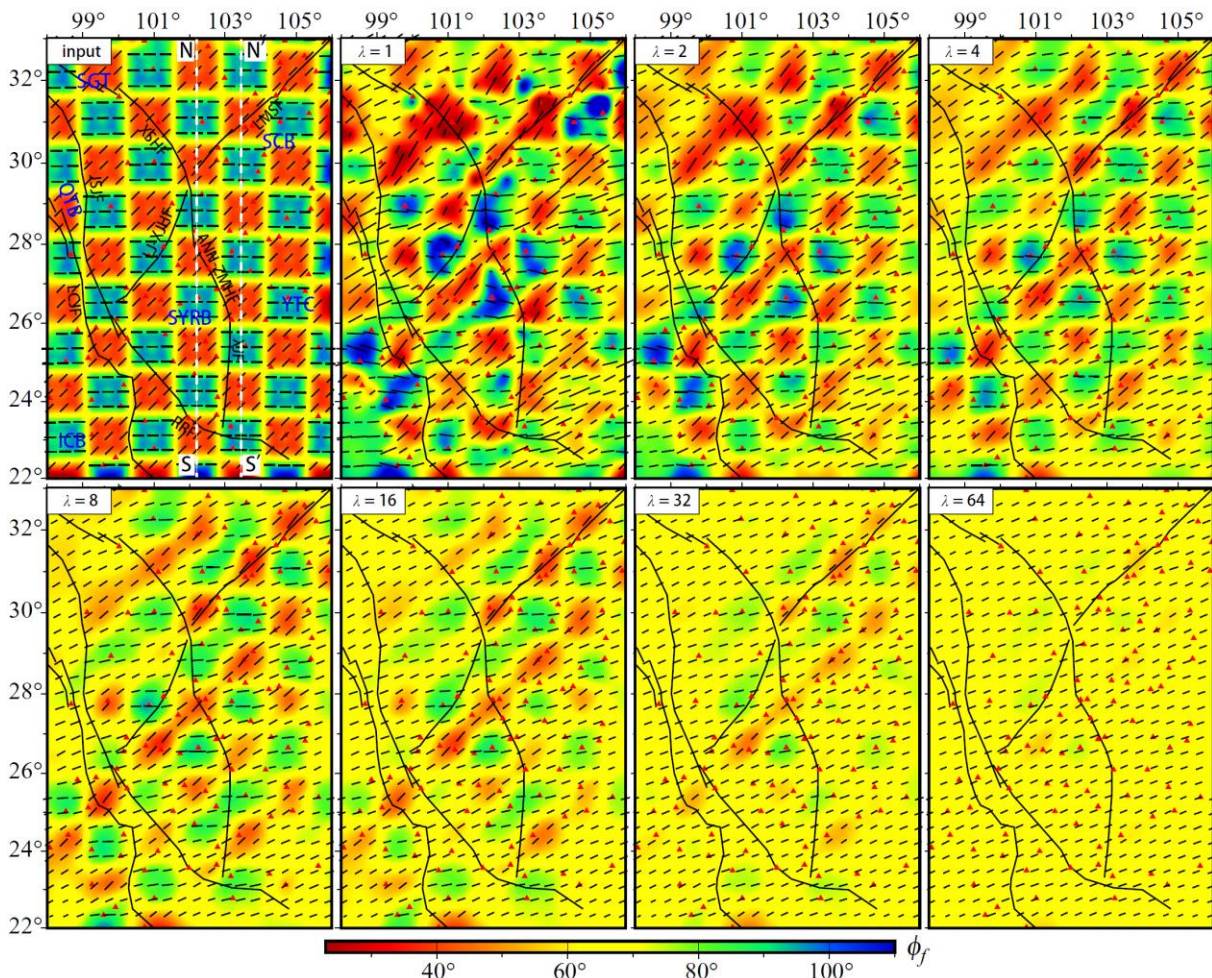
275 model can be obtained by an inverse wavelet transform. Readers may refer to Hung et al. (2011) for  
276 implementation details of the multi-scale parameterization. The wavelet approach achieves a higher spatial  
277 resolution where path coverage is better and a poorer resolution in less well-sampled regions, leading to  
278 results with objective and data-driven multi-scale resolution.

#### 279 **2.4 Resolution tests**

280 Careful selection of the damping factor  $\lambda$  and objectively evaluating the resolution for a given dataset in  
281 an inversion problem are paramount to interpreting the inversion results. Thus, it is important to characterize  
282 how reliable our anisotropic models are, and to limit our interpretations to robust features that are well-  
283 resolved and well-constrained by the observations.

284 We present three sets of resolution tests to illustrate the selection of the optimal damping factor and  
285 the resulting resolution of our SI dataset. In each resolution test, an input model is constructed for an  
286 assumed spatial variation of anisotropy strength  $\gamma$  and azimuth  $\phi_f$ . Then, the spatial distributions of  $\gamma_c$   
287 and  $\gamma_s$  are obtained from  $\gamma$  and  $\phi_f$ , and synthetic SI data for the input model are calculated for all SKS  
288 paths in our final dataset by integrating the products of the 3D sensitivity kernels  $K_{\gamma_c}^S$  and  $K_{\gamma_s}^S$  with  $\gamma_c$  and  
289  $\gamma_s$  according to Eq. (4). Gaussian noise with the same standard deviation as our final inversion dataset  
290 (0.074 s) is added to the synthetic SI data. We first perform a series of tests using checkerboards of two  
291 different sizes ( $1^\circ \times 1^\circ$  and  $1.5^\circ \times 1.5^\circ$ ) with horizontally alternating azimuthal angles of fast axes  $\phi_f =$   
292  $90^\circ$  and  $\phi_f = 45^\circ$  but a fixed anisotropy strength  $\gamma = 4\%$ . Figure 8 shows the input and recovered models  
293 for different values of the damping factor  $\lambda$  at a depth of 55 km for the  $1^\circ \times 1^\circ$  checkerboard test. The  
294 effect of damping factor on the anisotropy pattern in the inversion result is obvious. The recovery results  
295 suggest an optimal damping factor of  $\lambda = 4$ , and the checkerboard pattern is well-resolved in most parts  
296 of the study area except in the northwest and southeast corners where stations are more sparse. Results for  
297 the recovered models at different depths as well as for  $1.5^\circ \times 1.5^\circ$  checkerboards are presented in Figures

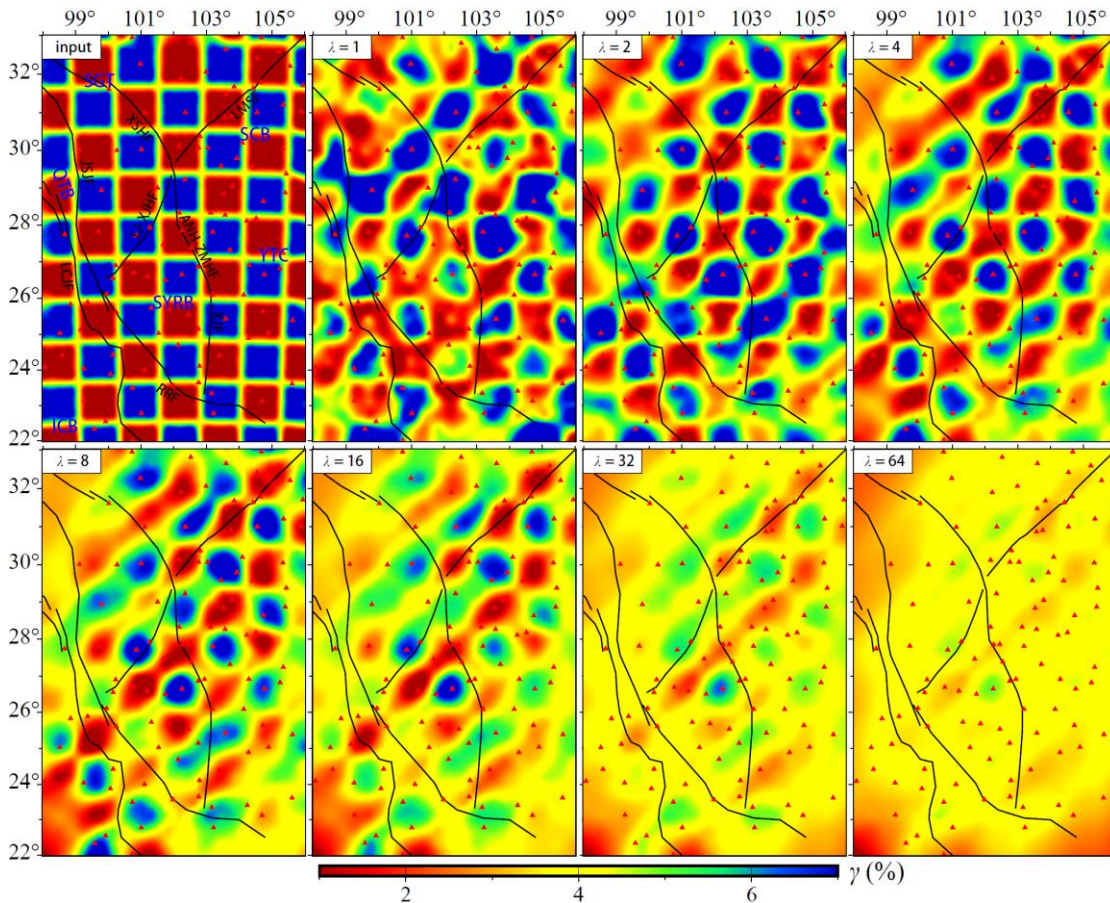
298 S1 and S2 in Supporting Information. Results of similar tests with alternating orthogonal azimuths of the  
 299 fast axis are presented Figures S3 and S4 in Supporting Information.



300  
 301 **Figure 8.** Resolution tests for the azimuth of symmetry axis using  $1^\circ \times 1^\circ$  checkerboard. (Top-left) The  
 302 input model has horizontally alternating azimuthal angles of fast axes  $\phi_f = 90^\circ$  and  $\phi_f = 45^\circ$  shown by  
 303 both the color and the directions of the line segments, and a fixed anisotropy strength  $\gamma = 4\%$  represented  
 304 by the lengths of the line segments. The two white dashed lines show the locations of profiles NS and N'S'  
 305 in Figure 11. The other panels show the recovered models at a depth of 55 km for different damping  
 306 factors  $\lambda$ . We choose  $\lambda = 4$  as the optimal value for the damping factor (top-right panel). Red triangles  
 307 show locations of stations used.

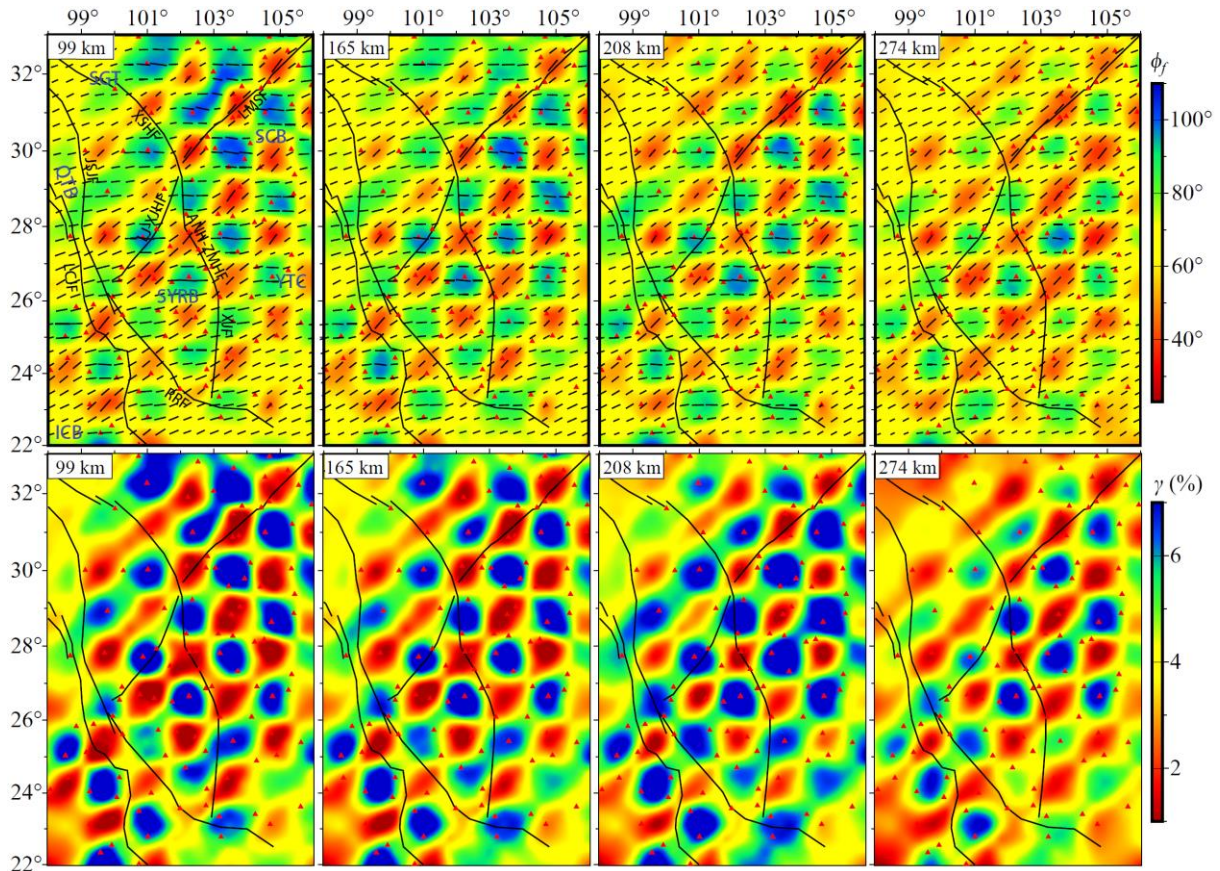
308 In the second set of tests, we use input checkerboard models with a fixed azimuthal angle of symmetry  
 309 axis  $\phi_f = 22.5^\circ$  but alternating perturbations of anisotropy strength of  $\delta\gamma = \pm 3\%$  relative to a

310 background anisotropy strength of  $\gamma = 4\%$ . Figure 9 shows the recovery results at the depth of 55 km  
 311 using different damping factors for the  $1^\circ \times 1^\circ$  input checkerboard model. Results for the recovered models  
 312 at different depths as well as for  $1.5^\circ \times 1.5^\circ$  checkerboards are presented in Figures S5 and S6 in Supporting  
 313 Information.



314  
 315 **Figure 9.** Resolution test using  $1^\circ \times 1^\circ$  checkerboard. (Top-left) The input model has horizontally  
 316 alternating anisotropy strengths shown by the colors representing perturbations of  $\delta\gamma = \pm 3\%$  relative to  
 317 a background anisotropy strength of  $\gamma = 4\%$ , and a fixed azimuthal angle of symmetry axis  $\phi_f = 22.5^\circ$ .  
 318 The other panels show the recovered models at a depth of 55 km for different damping factors  $\lambda$ . We  
 319 choose  $\lambda = 4$  as the optimal value for the damping factor (top-right panel).

320 The tests in Figures 8 and 9 both show that the damping factor of  $\lambda = 4$  yields the best resolved  
 321 checkerboard pattern. For convenience, resolution test results at different depths for damping factor  $\lambda =$   
 322 4 are collected and displayed in Figure 10.



323

324 **Figure 10.** Resolution test using  $1^\circ \times 1^\circ$  checkerboard with damping factor  $\lambda = 4$ . (Upper panels)  
 325 Recovered model at the depths of 99 km, 165 km, 208 km and 274 km for an input model having  
 326 horizontally alternating azimuthal angles of fast axes  $\phi_f = 90^\circ$  and  $\phi_f = 45^\circ$  with a fixed anisotropy  
 327 strength  $\gamma = 4\%$ . The input model and the recovered model at 55-km depth are shown in Figure 8. (Lower  
 328 panels) Recovered model at the depths of 99 km, 165 km, 208 km and 274 km for an input model with  
 329 horizontally alternating anisotropy strengths of  $\gamma = 1\%$  and  $\gamma = 7\%$  (perturbations of  $\delta\gamma = \pm 3\%$   
 330 relative to a background anisotropy strength of  $\gamma = 4\%$ ) with a fixed azimuthal angle of symmetry axis  
 331  $\phi_f = 22.5^\circ$ . The input model and the recovered model at 55-km depth are shown in Figure 9.

332

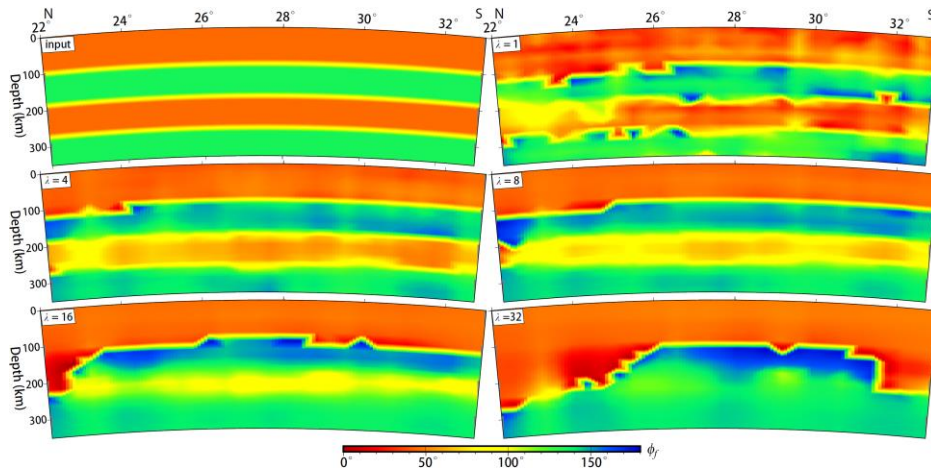
333

334

335

336

The third set of tests is intended to probe the depth resolution of our SI dataset with full-waveform  
 anisotropy tomography. We use input models with a fixed anisotropy strength of  $\gamma = 4\%$  but several  
 layers of alternating azimuthal angles of symmetry axes. Figure 11 shows the recovery results for a 4-  
 layer input model along a north-south vertical cross-section (cross-section NS in the top-left panel of  
 Figure 8) for different damping factors.



337

338 **Figure 11.** Resolution tests for an input model with 4 layers of alternating azimuthal angles of symmetry  
 339 axes  $\phi_f = 45^\circ$  and  $\phi_f = 135^\circ$  but a fixed anisotropy strength of  $\gamma = 4\%$ . Shown here are the input model  
 340 (top-left panel) and recovered models for different damping factors  $\lambda$  along the north-south cross-section  
 341 NS through the middle of the study region (see top-left panel in Figure 8). The optimal damping is  $\lambda = 4$   
 342 (middle-left panel).

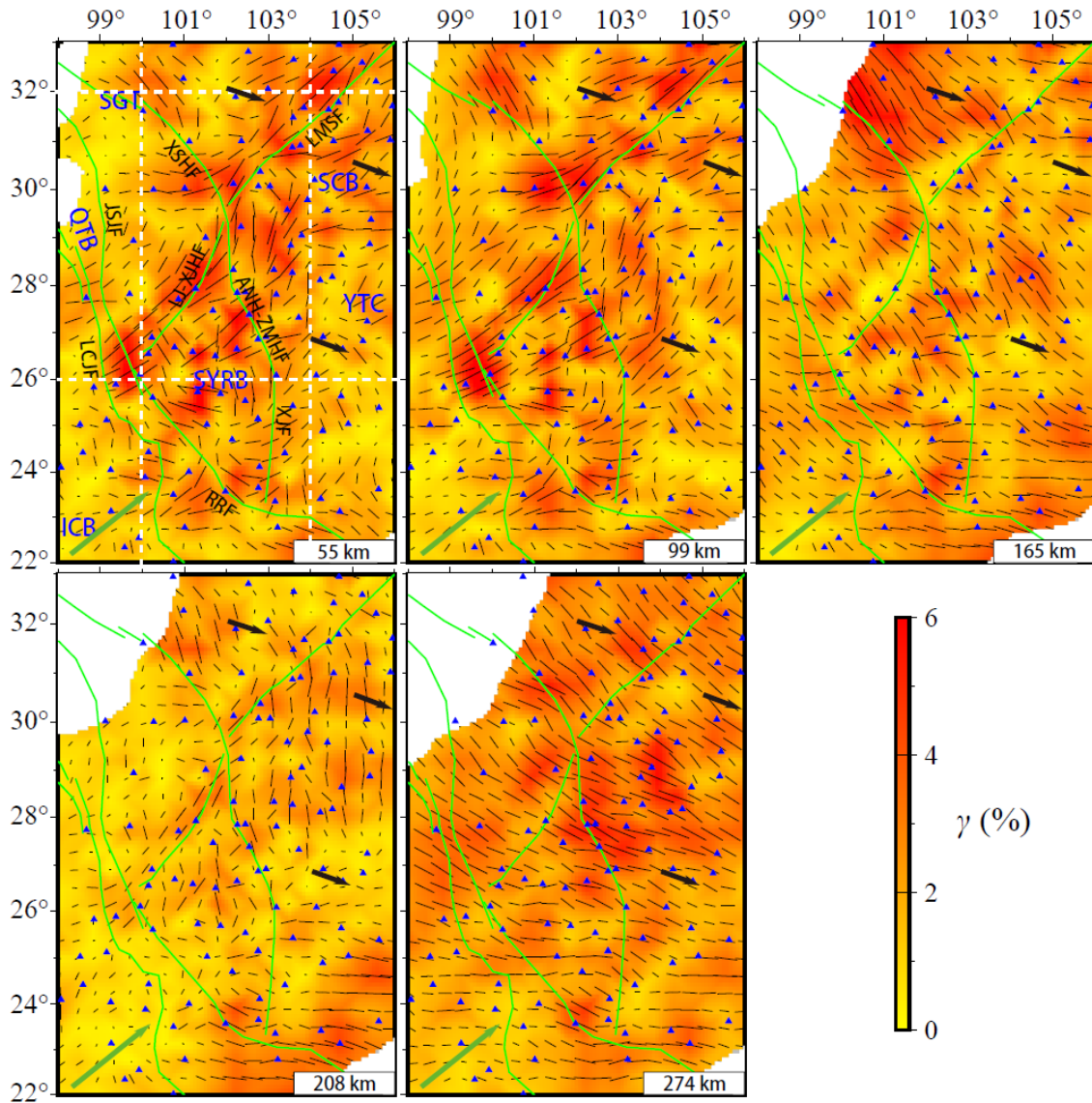
343 Recovered models along another profile as well as for a 2-layer input model are presented in  
 344 Supporting Information (Figures S7-S10). These results also suggest an optimal damping factor of  $\lambda = 4$ .  
 345 Based on all the resolution test results, we determine  $\lambda = 4$  to be the optimal damping factor for the SI  
 346 data inversions in this study. It should be noted that the noise level in the SI measurements can affect the  
 347 choice of the damping factor. The higher the noise level, the larger the damping factor (see the tests in  
 348 Figures S11–S14).

349 The above resolution tests demonstrate that with the available distributions of seismic stations and  
 350 teleseismic earthquakes, our SKS wave SI dataset can resolve reasonably well the shear-wave azimuthal  
 351 anisotropy with a horizontal dimension of  $1^\circ \times 1^\circ$  and a vertical thickness of  $\sim 100$  km in the main part of  
 352 the study region. Near the western border and in the SE corner, the resolution is poor due to larger station  
 353 spacing and fewer crossing SKS ray paths.

### 354 **3 Result**

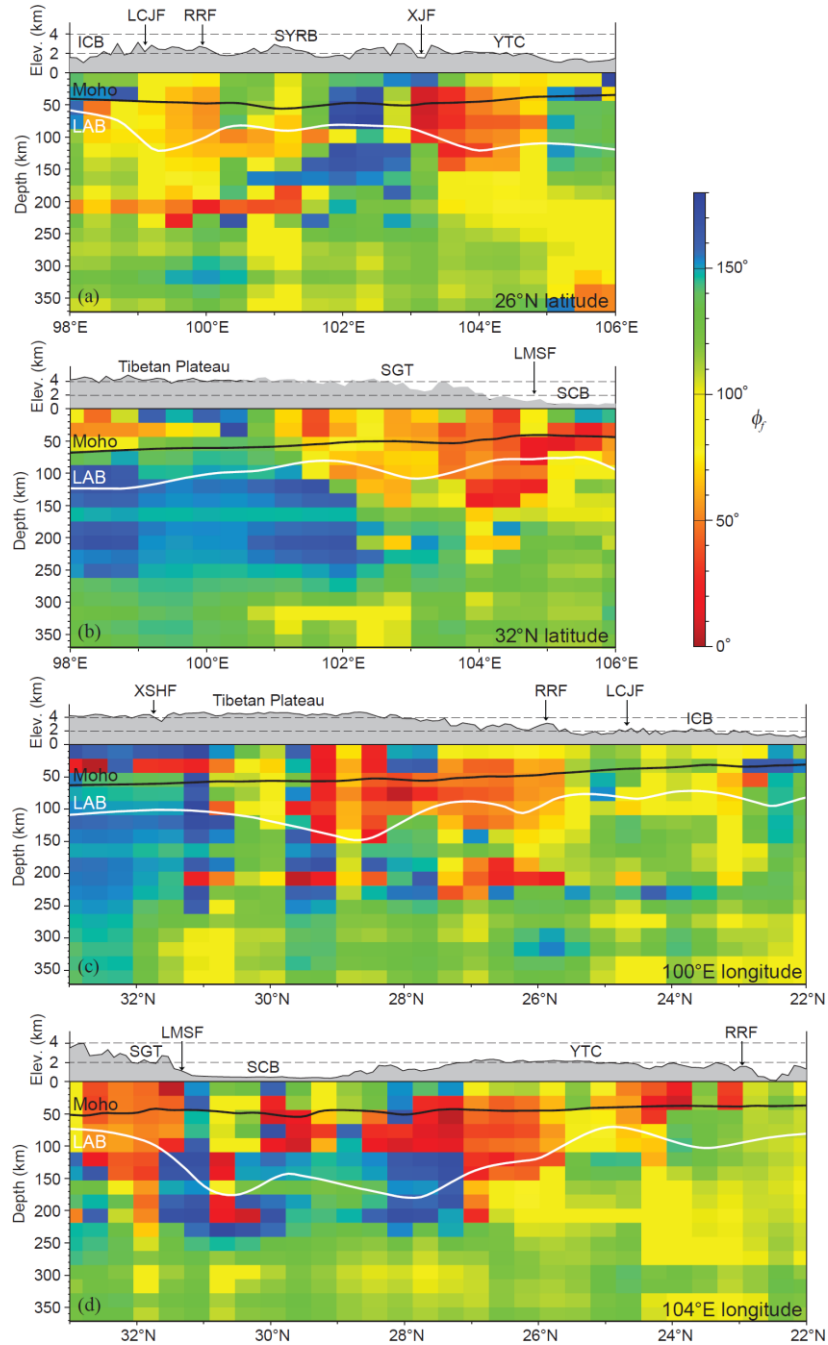
355 As stated in Section 2.2, our final dataset contains 5,216 SI measurements at 111 permanent seismic

356 stations from 470 events, which are used to invert for the 3D azimuthal anisotropy structure of the study  
 357 region. Figure 12 displays our inverted model at five representative depths. The azimuths of fast axis along  
 358 four vertical profiles are shown in Figure 13.



359  
 360 **Figure 12.** Three-dimensional anisotropic model for the SE margin of Tibetan Plateau at 55 km, 99 km,  
 361 165 km, 208 km and 274 km depths. The anisotropy strength and the azimuth of the fast axes are shown  
 362 by the background color and the black line segments, respectively. The lengths of the line segments are  
 363 proportional to the anisotropy strength. The black and green arrows denote the absolute plate motion  
 364 (APM) of the Eurasian and Indian plates, respectively, according to the model NNR-MORVEL56 (Argus  
 365 et al., 2011). The white dashed lines show locations of the profiles shown in Figure 13. Names of major

366 faults and tectonic blocks are the same as in Figure 1. Blue triangles show locations of stations used.  
 367 Regions in which the recovery errors are above 20% are mask out. The recovery error is defined by  $E =$   
 368  $(|\phi_f - \tilde{\phi}_f|/90^\circ) \times 100\%$ , where  $\tilde{\phi}_f$  and  $\phi_f$  are the input and recovered azimuthal angles in the  
 369 resolution tests in Figures 8 and 10.



370  
 371 **Figure 13.** Vertical profiles of the azimuths of fast axis in our 3D anisotropy model along (a) 26°N latitude,  
 372 (b) 32°N latitude, (c) 100°E longitude and (d) 104°E longitude. The azimuths of the fast axis are shown by

373 the background color. Note that red ( $\sim 0^\circ$ ) and blue ( $\sim 180^\circ$ ) colors both indicate nearly N-S fast axis,  
374 whereas yellow color indicates nearly E-W fast axis. Moho and lithosphere-asthenosphere boundary (LAB)  
375 are depicted by thick black and white lines, respectively. Names of major faults and tectonic blocks are  
376 the same as in Figure 1.

377 As a first check of the inversion result, we calculate the model-predicted conventional SKS splitting  
378 time  $\Delta t$  and fast-direction azimuth  $\theta$  by integrating the anisotropy model (Figure 12) with sensitivity  
379 kernels (Figure 7) according to Eq. (4) and compare with observations. The comparison in Figure 6 shows  
380 excellent agreement between the model-predicted splitting parameters with observations at all stations.

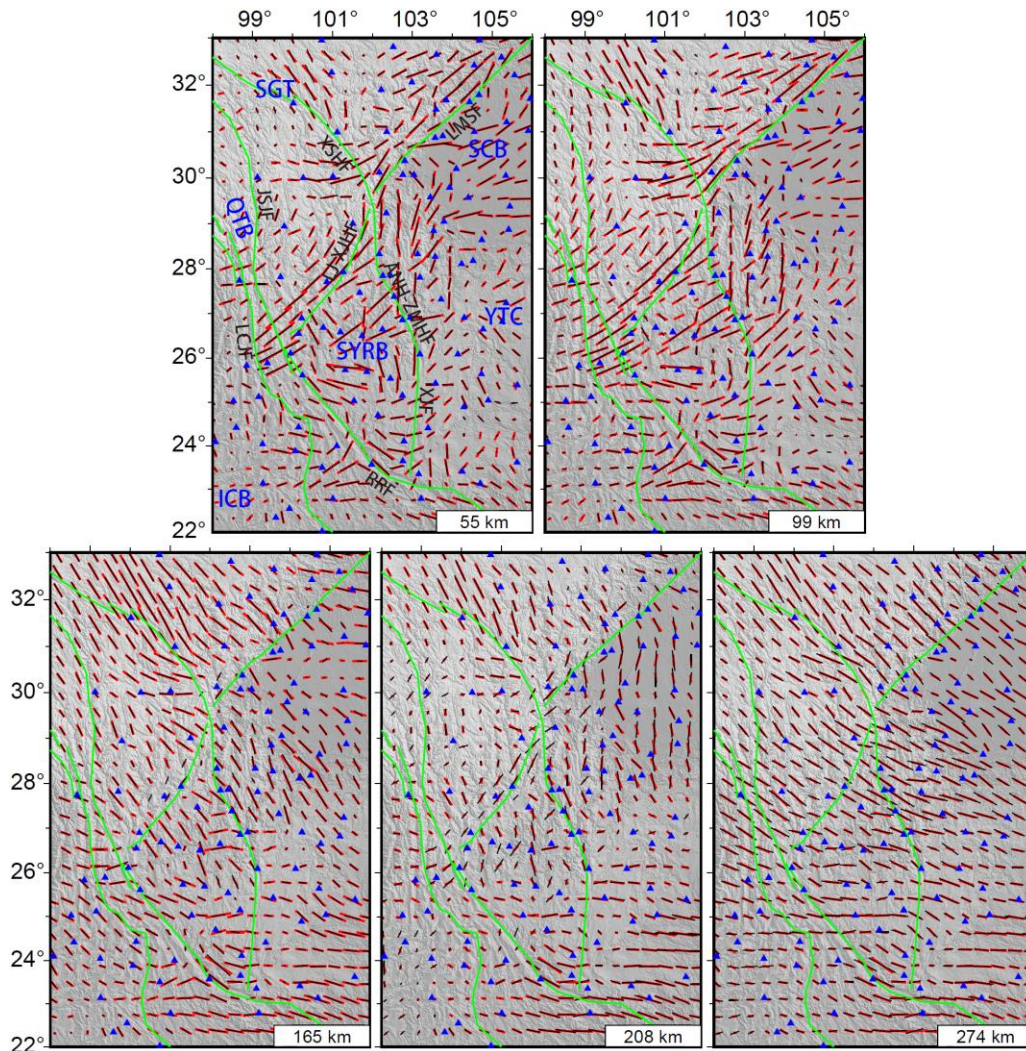
381 We also carry out a recovery test for our inversion result, in which we use the model in Figure 12 as  
382 the input model and calculate the synthetic SI data, then invert them using the same model discretization  
383 and damping factor as in the inversion of the real data. The comparison in Figure 14 shows that the output  
384 model strongly resembles the input model at all depths. The synthetic inversion successfully reproduces all  
385 the major features of the input model.

## 386 **4 Discussion**

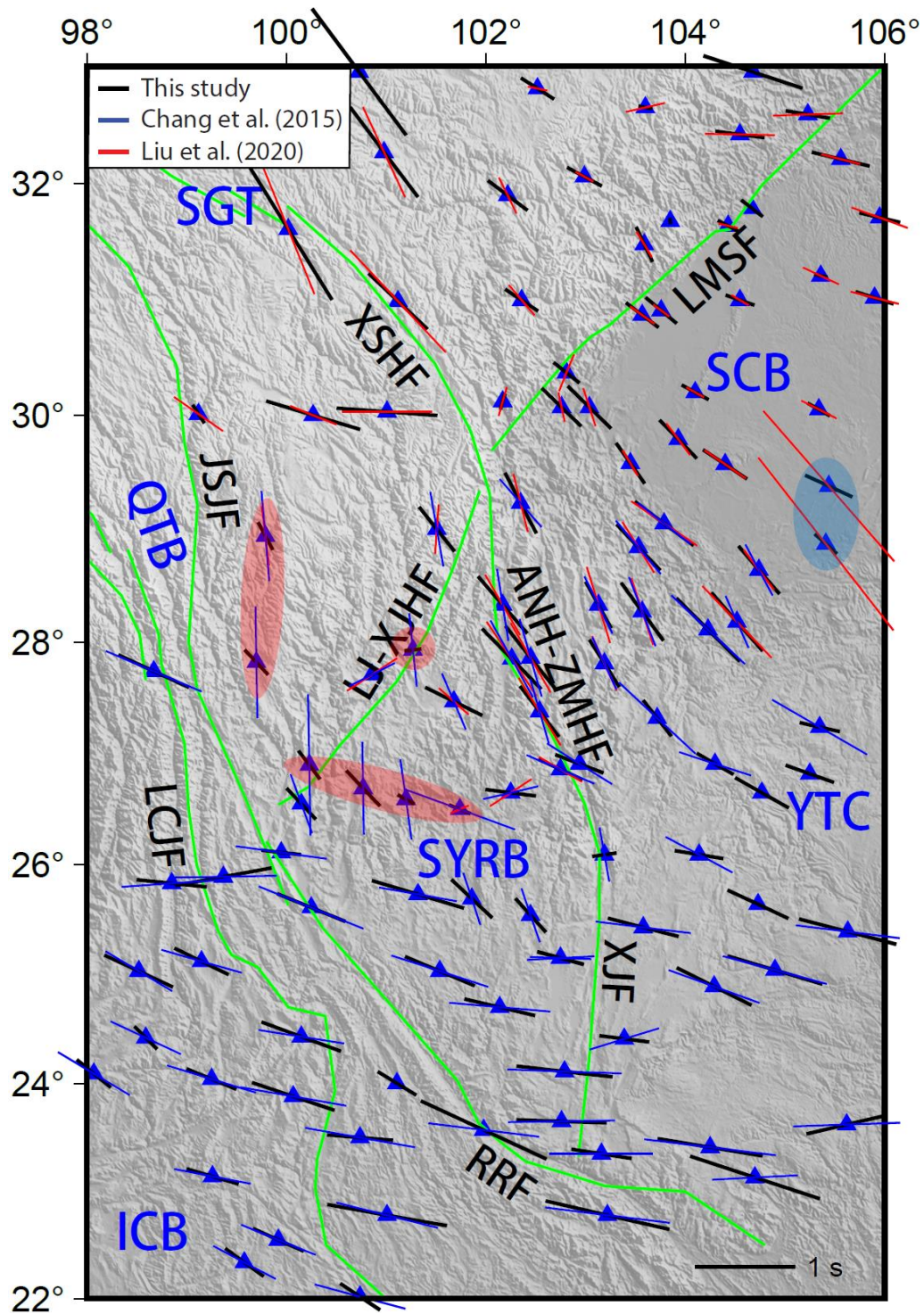
### 387 **4.1 Comparison with previous results**

388 SKS splitting observation has been widely used to investigate the upper mantle anisotropy in the SE margin of  
389 Tibetan Plateau (e.g., Lev et al., 2006; Flesch et al., 2005; Wang et al., 2008; Shi et al., 2012; Chang et al., 2015;  
390 Yang et al., 2018; Liu et al., 2020; Huang & Chevrot, 2021; Li et al., 2021). In Figure 15, we compare our  
391 splitting result with those of Chang et al. (2015) and Liu et al. (2020) whose SKS splitting data are available  
392 from the Shear Wave Splitting Product Query website (<http://ds.iris.edu/spud/swsmeasurement>). At most  
393 stations, predictions by our model are consistent with both studies. Major differences occur at two stations at  
394 the southern tip of SCB (highlighted by the blue ellipse in Figure 15), where anomalously large splitting times  
395 can be seen in the results of Liu et al. (2020), shown by the red line segments. There are also discrepancies in  
396 both delay time and fast-axis azimuth at a few stations across the LJ-XJHF (highlighted by the red ellipses in

397 Figure 15) where Chang et al. (2015) reported large splitting times and nearly N-S fast axes, whereas our model  
 398 predicts moderate-to-small splitting times and more E-W orientation of fast axes. Note that a strictly quantitative  
 399 comparison of different studies is difficult due to differences in earthquake and window selections, data  
 400 processing and frequency bands used in the measurement of SKS splitting parameters.



401  
 402 **Figure 14.** Result of the recovery test. The recovered and input anisotropic models are compared at five  
 403 depths marked at the bottom-right corner in each panel. Black and red line segments denote the directions  
 404 of fast axes in the input and recovered models, respectively, and their lengths indicates the anisotropy  
 405 strength. Names of major faults and tectonic blocks are the same as in Figure 1. Blue triangles show  
 406 locations of stations used.



407

408 **Figure 15.** Comparison of SKS splitting times and fast axis directions predicted by our anisotropy model  
 409 (Figure 12) with previous studies. Black line segments are results from the present study, whereas blue and red  
 410 line segments show results from Chang et al. (2015) and Liu et al. (2020), respectively. Blue and red ellipses  
 411 highlight stations where there are large discrepancies in splitting parameters between this study and Liu et al.

412 (2020) and Chang et al. (2015), respectively. Names of major faults and tectonic blocks are the same as in  
413 Figure 1.

414 Depth variation of anisotropy can also be investigated by surface-wave tomography studies (e.g.  
415 Montagner & Nataf, 1986; Debayle et al., 2005; Lin et al., 2011). Bao et al. (2020) and Zhang et al. (2023)  
416 used Rayleigh-wave dispersion curves measured from ambient noise and teleseismic earthquakes to invert  
417 for the azimuthal anisotropy in the SE margin of Tibetan Plateau. In general, both surface-wave results  
418 show a lower anisotropy strength of 2–3% with smoother spatial variation patterns than our model  
419 obtained from SKS splitting intensity. At the relatively shallow depths (~55 km) in the vicinity of the  
420 LMSF and LJ-XJHF, all models exhibit fast axes nearly parallel to the fault zones. Surface-wave  
421 tomography acquires depth resolution from different depth distributions of sensitivity of surface waves of  
422 different frequencies, but its horizontal resolution is limited due to the horizontal averaging of horizontally  
423 propagating surface waves. In addition, almost all surface-wave tomography studies use fundamental  
424 Rayleigh waves, which also limits the depth resolution. On the other hand, our fullwave SI inversion uses  
425 nearly vertically propagating SKS waves, which acquires spatial resolution from the 3D sensitivity kernels  
426 (Figure 7) with higher resolution horizontally than vertically. Therefore, discrepancies between models  
427 obtained by surface-wave dispersion and SKS SI can be expected given the current station distribution  
428 and available data.

#### 429 **4.2 Overall variation of shear-wave anisotropy**

430 Our anisotropy model exhibits an overall anisotropy strength  $\gamma$  of up to 6% in the lithosphere and  
431 asthenosphere. Both the strength and fast-axis show strong lateral and vertical variations (Figures 12 and  
432 13). Within the lithosphere (depths of 55 km and 99 km), the anisotropy is strong in the vicinity of the  
433 LMSF and LJ-XJHF, the major fault zones in the region that form the boundary between the Tibetan  
434 Plateau and the YTC. At greater depths in the asthenosphere (e.g. 274 km), the entire region exhibits  
435 strong anisotropy with a largely NW-SE fast axis (predominantly green color in the lower parts in Figure

436 13), parallel to the direction of GPS observed surface velocity (Figure 1) and the APM (black arrows in  
437 Figure 12), and turns to more E-W south of  $\sim 26^\circ\text{N}$ . At intermediate depths (165 km and 208 km), the  
438 anisotropy is highly variable, both in strength and direction of symmetry axis. Therefore, our model shows  
439 an apparent decoupling of lithosphere and asthenosphere deformation in the SE margin of Tibetan Plateau,  
440 consistent with previous studies (e.g. Flesch et al., 2005).

441 Most previous studies have reported two major features in the SKS splitting pattern in the region: an overall  
442 NW-SE fast axis and an E-W alignment of fast axes south of  $\sim 26^\circ\text{N}$  latitude (e. g., Lev et al., 2006; Wang et  
443 al., 2008; Chang et al., 2015; Huang & Chevrot, 2021), as shown in Figures 6 and 15. Our model shows that  
444 this relatively simple splitting pattern observed at seismic stations on the surface is a manifestation of the vertical  
445 averaging of complex variation of anisotropy over lithospheric and asthenospheric depths. For instance, along  
446 the LMSF, the fast axes in the lithospheric depths (e.g. 55 km and 99 km) are mainly oriented NE-SW with  
447 relatively high anisotropy strength, but change to NW-SE in the asthenosphere. As a result, we observe  
448 relatively small SKS splitting times ( $< 0.5$  s) with a NW-SE fast axis at the surface. On the other hand, the  
449 moderate SKS splitting times (1 s or less) and E-W alignment of fast axes south of  $\sim 26^\circ\text{N}$  are resulted primarily  
450 from a strong E-W azimuthal anisotropy (green and yellow colors south of  $26^\circ\text{N}$  and below the LAB in  
451 Figures 13c and 13d) generated by an E-W asthenospheric flow due to the eastward subduction of the  
452 Indian Plate under Myanmar (e.g. Yang et al., 2022). Regional variation of lithospheric and asthenospheric  
453 contributions to anisotropy leads to small but discernable differences in SKS splitting observations. For  
454 example, under the SYRB, the anisotropy in the lithosphere between  $24^\circ\text{N}$  and  $26^\circ\text{N}$  is relatively strong  
455 (55 km and 99 km depths in Figure 12) with different orientations of fast axes. The vertical integration of  
456 lithospheric and asthenospheric anisotropy results in horizontally variable SKS splitting times and fast  
457 axes observed at seismic stations on the surface, as shown by the stations in SYRB in Figures 6 and 15.  
458 In the rest of the study region south of  $26^\circ\text{N}$ , the asthenospheric contribution dominates, and the surface

459 SKS splitting parameters exhibit relatively uniform E-W fast axes.

### 460 **4.3 The Songpan-Ganzi Terrane**

461 In our study region, the SGT is bounded by the JSJF in the southwest and LMSF and LJ-XJHF in the  
462 southeast (Li et al., 2021). In the eastern margin of the SGT, the eastward expansion of the Tibetan Plateau  
463 is blocked by the SCB, part of the YTC. Our model shows two distinct types of anisotropy. In the area far  
464 away from the LMSF, the anisotropy is moderate to strong (3–6%) with NW-SE fast axes in both  
465 lithosphere and asthenosphere (light blue and green colors under Tibetan Plateau in Figures 13b and 13c),  
466 parallel to the GPS surface velocity (Figure 1), the regional APM direction (black arrows in Figure 12)  
467 and the asthenospheric flow, suggesting a vertical coupling of deformation there, in agreement with Flesch  
468 et al. (2005). The NW-SE anisotropy in the SGT is consistent with previous tomography results from  
469 Rayleigh waves (Legendre et al., 2015; Bao et al., 2020) and Pn waves (Lei et al., 2014). However, in the  
470 area near the LMSF, the fast axis in the lithosphere (e.g. 55 km and 99 km depths) becomes NE-SW,  
471 parallel to the proposed lithospheric material flow as a result of the resistance of SCB to the eastward  
472 expansion of the Tibetan Plateau at LMSF. Near the LMSF, lithospheric material of the SGT appears to  
473 diverge at  $\sim 102^\circ$  longitude, going in opposite directions (NE and SW). In the asthenosphere, the fast axis  
474 returns to NW-SE, consistent with the regional APM. The relatively sharp turn of the fast axis in the  
475 lithosphere from SE-NW to NE-SW at the southern tip of SGT is a clear evidence for the redirection of  
476 the lithospheric flow from eastward to southward in the SE margin of Tibetan Plateau.

### 477 **4.4 The Yangtze Craton**

478 The YTC is a Precambrian continental block which was accreted to the North China Craton in the Triassic. Our  
479 study region covers the western margin of the YTC, namely the SCB and SYRB, and our model shows  
480 that the anisotropy in the region varies significantly both horizontally and vertically, as a result of the  
481 complex geodynamic evolution of the YTC involving multiple rounds of lithospheric reactivation, such

482 as the Permian-Triassic Emeishan flood basalt eruption (e.g. Xu et al., 2001), as well as interactions with  
483 surrounding tectonic blocks. In our model, the SCB exhibits a moderate anisotropy with a NE-SW orientation  
484 near the LMSF at shallow depths (e.g. 55 km and 99 km depths in Figure 12 and yellow and red colors  
485 under LMSF in Figure 13b), presumably the effect of a dominant shearing in the vicinity of the LMSF by  
486 the moving SGT lithosphere in NE and SW directions. Further east, E-W compression gradually takes  
487 over the NE-SW shear at shallow depths, and the fast axis of anisotropy turns to more E-W (e.g. 55 km,  
488 99 km and 165 km). This turn of anisotropy from NE-SW to more E-W away from the LMSF has also  
489 been observed in surface-wave studies (e.g. Zhang et al., 2023). At greater depths in the lithosphere (208  
490 km in Figure 12 and red and blue colors under SCB in Figure 13d), the anisotropy under the SCB becomes  
491 nearly N-S, which is consistent with a frozen anisotropy in the lithosphere generated by the mantle flow  
492 in the Cenozoic (Li et al., 2021) without being modified by the SGT-SCB block interaction at shallower  
493 depths. At asthenospheric depths (274 km), the anisotropy is largely aligned with the regional APM.

494 The anisotropy under the SYRB appears to be continuous across the ANH-ZMHF and XJF,  
495 suggesting that both fault systems are crustal boundaries where the SYRB is escaping in the SE direction.  
496 In the lithosphere (55 km and 99 km under SYRB and above 208 km depth east of ANH-ZMHF between  
497 the SCB and 26°N), the anisotropy has a complex pattern of relatively small-scale horizontal variations of  
498 fast axes, perhaps a result of multiple phases of lithospheric reactivations that have modified the previously  
499 frozen anisotropy. In the asthenosphere (> 100 km depth in SYRB and > 200 km between the SCB and  
500 26°N), the anisotropy largely follows the direction of the regional APM or mantle flow. Around 208-km  
501 depth, the azimuthal anisotropy south of the SCB is very weak, which may indicate a more complex local  
502 mantle flow pattern due to the regionally predominant NW-SE mantle flow being disturbed by the root of  
503 the YTC lithosphere. South of 26°N, the anisotropy under the YTC returns to largely parallel to the  
504 direction of APM.

## 505 **5 Conclusions**

506 In this study, we have carried out fullwave multiscale tomography to obtain a 3D model for the shear-  
507 wave anisotropy in the SE margin of Tibetan Plateau. A total of 5,216 high-quality SKS splitting  
508 intensities are obtained from the broadband records of 470 teleseismic events at 111 permanent stations  
509 after a series of quality control measures. In conjunction with the 3D sensitivity kernels and a wavelet-  
510 based parameterization, the splitting intensities are inverted to achieve a data-driven multi-scale resolution  
511 to anisotropy structure in the upper mantle.

512 The vertical variation of the anisotropy in our result indicates that the lithospheric and asthenospheric  
513 deformations are decoupled in the SE margin of the Tibetan Plateau. On the other hand, the anisotropy  
514 appears to be vertically consistent under the Songpan-Ganzi Terrane, suggesting a coupling of the  
515 deformations in the lithosphere and asthenosphere in the interior of the Tibetan Plateau. It is worthwhile  
516 to point out that the vertical resolution is limited due to the nearly vertical propagation of the SKS waves.  
517 As a result, the Moho discontinuity and crustal anisotropy are poorly resolved in our anisotropy model.

518 The strength of anisotropy in our model is spatially variable and can reach 6%, with strongest  
519 anisotropy in the asthenosphere presumably due to large-scale and relatively steady mantle flow, and in  
520 the lithosphere in the vicinity of the Longmenshan Fault and Lijiang-Xiaojinhe Fault, probably due to  
521 large shearing effect generated by the relative movement between the Songpan-Ganzi Terrane and the  
522 Sichuan Basin.

523 The azimuth of the fast axis of anisotropy in the asthenosphere largely follows the direction of regional  
524 absolute plate motion or mantle flow, i.e. mostly southeastward beneath the Songpan-Ganzi Terrane and the  
525 Yangtze Craton and nearly east-west south of 26°N latitude. In the lithosphere, however, the fast axis is highly  
526 variable. In the Sichuan Basin, the frozen anisotropy dominates in the deep lithosphere; whereas at shallower  
527 depths, the anisotropy is modified by the interaction with the Songpan-Ganzi Terrane into southeastward in the

528 vicinity of the Longmenshan Fault and nearly east-west further east. In the Sichuan-Yunnan Rhombic Block  
529 and east of the Anninghe-Zemuhe Fault, the azimuth of the fast axis of anisotropy exhibits complex spatial  
530 pattern due to multiple phases of lithospheric reactivation. The vertical integration of the contributions from  
531 complex lithospheric anisotropy and relatively uniform asthenospheric anisotropy gives rise to the  
532 seemingly simple pattern of conventional SKS splitting parameters observed at the surface. Our 3D model  
533 of azimuthal anisotropy provides important new insights into the lithospheric and asthenospheric  
534 dynamics in the SE margin of Tibetan Plateau.

535

536

### 537 **Acknowledgments**

538 We sincerely thank the two anonymous reviewers for their critical reviews and constructive comments  
539 which greatly helped improve the manuscript. This work has been supported by the National Natural  
540 Science Foundation of China (NSFC Grants U1939202 and 41974046). Y.L. has been supported by the  
541 68th China Postdoctoral Science Foundation under Grant 2020M680205. Most of the figures are generated  
542 using the Generic Mapping Tools (Wessel et al., 2019, <https://www.generic-mapping-tools.org>).

543

### 544 **Open Research**

545 The raw waveform data, the measured splitting intensities as well as the obtained anisotropic model can  
546 be accessed at Lin, Y., & Zhao, L. (2024).

547 **References**

- 548 Argus, D. F., Gordon, R. G., & DeMets, C. (2011). Geologically current motion of 56 plates relative to  
549 the no-net-rotation reference frame. *Geochemistry, Geophysics, Geosystems*, 12(11). doi:  
550 10.1029/2011GC003751
- 551 Bao, X., Song, X., Eaton, D. W., Xu, Y., & Chen, H. (2020). Episodic lithospheric deformation in eastern  
552 Tibet inferred from seismic anisotropy. *Geophysical Research Letters*, 47(3). doi:  
553 10.1029/2019gl085721
- 554 Becker, T. W., Chevrot, S., Schulte-Pelkum, V., & Blackman, D. K. (2006). Statistical properties of  
555 seismic anisotropy predicted by upper mantle geodynamic models. *Journal of Geophysical Research:*  
556 *Solid Earth*, 111(B8). doi: 10.1029/2005JB004095
- 557 Cai, Y., Wu, J., Fang, L., Wang, W., & Yi, S. (2016). Crustal anisotropy and deformation of the  
558 southeastern margin of the Tibetan Plateau revealed by Pms splitting. *Journal of Asian Earth*  
559 *Sciences*, 121, 120–126. doi: 10.1016/j.jseae.2016.02.005
- 560 Chang, L.-J., Ding, Z.-F., & Wang, C.-Y. (2015). Upper mantle anisotropy beneath the southern segment  
561 of north-south tectonic belt, China. *Chinese Journal of Geophysics (in Chinese)*, 58(11), 4052–4067.  
562 doi: 10.6038/cjg20151114
- 563 Chevrot, S. (2000). Multichannel analysis of shear wave splitting. *Journal of Geophysical Research: Solid*  
564 *Earth*, 105(B9), 21579–21590. doi: 10.1029/2000JB900199
- 565 Chevrot, S. (2006). Finite-frequency vectorial tomography: a new method for high-resolution imaging of  
566 upper mantle anisotropy. *Geophysical Journal International*, 165(2), 641–657. doi: 10.1111/j.1365-  
567 246X.2006.02982.x
- 568 Chiao, L. Y., & Kuo, B. Y. (2001). Multiscale seismic tomography. *Geophysical Journal International*,  
569 145(2), 517-527. doi: 10.1046/j.0956-540x.2001.01403.x
- 570 Dahlen, F., Hung, S.-H., & Nolet, G. (2000). Fréchet kernels for finite-frequency travel- times—I. Theory.  
571 *Geophysical Journal International*, 141(1), 157-174. doi: 10.1046/j.1365-246X.2000.00070.x
- 572 Debayle, E., Kennett, B., & Priestley, K. (2005). Global azimuthal seismic anisotropy and the unique  
573 plate-motion deformation of Australia. *Nature*, 433, 509-512.
- 574 Dziewonski, A. M., & Anderson, D. L. (1981). Preliminary reference Earth model, *Physics of the Earth*  
575 *and Planetary Interior*, 25, 297–356.
- 576 Favier, N., & Chevrot, S. (2003). Sensitivity kernels for shear wave splitting in transverse isotropic media.  
577 *Geophysical Journal International*, 153(1), 213–228. doi: 10.1046/j.1365-246X.2003.01894.x

- 578 Flesch, L. M., Holt, W. E., Silver, P. G., Stephenson, M., Wang, C.-Y., & Chan, W. W. (2005).  
579 Constraining the extent of crust–mantle coupling in central Asia using GPS, geologic, and shear wave  
580 splitting data. *Earth and Planetary Science Letters*, 238(1-2), 248-268. doi:  
581 10.1016/j.epsl.2005.06.023
- 582 Han, C., Xu, M., Huang, Z., Wang, L., Xu, M., Mi, N., Yu, D., Guo, T., Wang, H., Hao, S., Tia, M., &  
583 Bi, Y. (2020). Layered crustal anisotropy and deformation in the SE Tibetan Plateau revealed by  
584 Markov-Chain-Monte-Carlo inversion of receiver functions. *Physics of the Earth and Planetary*  
585 *Interiors*, 306, 106522. doi: 10.1016/j.pepi.2020.106522
- 586 Hu, J., Su, Y., Zhu, X., & Chen, Y. (2005). S-wave velocity and Poisson's ratio structure of crust in  
587 Yunnan and its implication. *Science in China Series D: Earth Sciences*, 48(2), 210–218. doi:  
588 10.1360/03yd0062
- 589 Huang, J., Zhao, D., & Zheng, S. (2002). Lithospheric structure and its relationship to seismic and volcanic  
590 activity in southwest China. *Journal of Geophysical Research: Solid Earth*, 107(B10), ESE–13. doi:  
591 10.1029/2000JB000137
- 592 Huang, P., Gao, Y., & Xue, B. (2022). Advances in the deep tectonics and seismic anisotropy of the  
593 Lijiang-Xiaojinhe fault zone in the Sichuan-Yunnan block, southwestern China. *Earthquake*  
594 *Research Advances*, 2(1), 100116. doi: 10.1016/j.eqrea.2022.100116
- 595 Huang, R., Wang, Z., Pei, S., & Wang, Y. (2009). Crustal ductile flow and its contribution to tectonic  
596 stress in Southwest China. *Tectonophysics*, 473(3-4), 476–489. doi: 10.1016/j.tecto.2009.04.001
- 597 Huang, Z., & Chevrot, S. (2021). Mantle dynamics in the SE Tibetan Plateau revealed by teleseismic  
598 shear-wave splitting analysis. *Physics of the Earth and Planetary Interiors*, 313, 106687. doi:  
599 10.1016/j.pepi.2021.106687
- 600 Huang, Z., Wang, L., Xu, M., & Zhao, D. (2018). P wave anisotropic tomography of the SE Tibetan  
601 Plateau: Evidence for the crustal and upper-mantle deformations. *Journal of Geophysical Research:*  
602 *Solid Earth*, 123(10), 8957–8978. doi: 10.1029/2018JB016048
- 603 Huang, Z., Zhao, D., & Wang, L. (2015). P wave tomography and anisotropy beneath Southeast Asia:  
604 Insight into mantle dynamics. *Journal of Geophysical Research: Solid Earth*, 120(7), 5154–5174.  
605 doi: 10.1002/2015JB012098
- 606 Hung, S. H., Chen, W. P., & Chiao, L. Y. (2011). A data-adaptive, multiscale approach of finite-frequency,  
607 travelt ime tomography with special reference to P and S wave data from central Tibet. *Journal of*  
608 *Geophysical Research: Solid Earth*, 116. doi: 10.1029/2010JB008190

- 609 Kind, R., Yuan, X., Saul, J., Nelson, D., Sobolev, S., Mechie, J., Zhao, W., Kosarev, G., Ni, J., Achauer,  
610 U., & Jiang, M. (2002). Seismic images of crust and upper mantle beneath Tibet: Evidence for  
611 Eurasian plate subduction. *Science*, 298(5596), 1219–1221. doi: 10.1126/science.1078115
- 612 Legendre, C. P., Deschamps, F., Zhao, L., & Chen, Q.-F. (2015). Rayleigh-wave dispersion reveals crust-  
613 mantle decoupling beneath eastern Tibet. *Scientific Reports*, 5(1), 1–7. doi: 10.1038/srep16644
- 614 Lei, J., Li, Y., Xie, F., Teng, J., Zhang, G., Sun, C., & Zha, X. (2014). Pn anisotropic tomography and  
615 dynamics under eastern Tibetan Plateau. *Journal of Geophysical Research: Solid Earth*, 119(3),  
616 2174–2198. doi: 10.1002/2013JB010847
- 617 Lev, E., Long, M. D., & van der Hilst, R. D. (2006). Seismic anisotropy in Eastern Tibet from shear wave  
618 splitting reveals changes in lithospheric deformation. *Earth and Planetary Science Letters*, 251(3-4),  
619 293-304. doi: 10.1016/j.epsl.2006.09.018
- 620 Li, H., Su, W., Wang, C.-Y., & Huang, Z. (2009). Ambient noise Rayleigh wave tomography in western  
621 Sichuan and eastern Tibet. *Earth and Planetary Science Letters*, 282(1-4), 201–211. doi:  
622 10.1016/j.epsl.2009.03.021
- 623 Li, W., Chen, Y., Liang, X., & Xu, Y.-G. (2021). Lateral seismic anisotropy variations record interaction  
624 between Tibetan mantle flow and plume-strengthened Yangtze Craton. *Journal of Geophysical  
625 Research: Solid Earth*, 126, e2020JB020841. <https://doi.org/10.1029/2020JB020841>
- 626 Lin, F., Ritzwoller, M. H., Yang, Y., Moschetti, M. P., & Fouch, M. J. (2011). Complex and variable  
627 crustal and uppermost mantle seismic anisotropy in the western United States, *Nature Geoscience*,  
628 4, 55–61.
- 629 Lin, Y., & Zhao, L. (2024). Upper-mantle anisotropy in the southeastern margin of Tibetan Plateau  
630 revealed by fullwave SKS splitting intensity tomography [Data set]. *Zenodo*.  
631 <https://doi.org/10.5281/zenodo.10668695>
- 632 Lin, Y.-P., Zhao, L., & Hung, S.-H. (2014a). Full-wave effects on shear wave splitting, *Geophysical  
633 Research Letters*, 41(3), 799–804. doi: 10.1002/2013GL058742
- 634 Lin, Y.-P., Zhao, L., & Hung, S.-H. (2014b). Full-wave multiscale anisotropy tomography in Southern  
635 California. *Geophysical Research Letters*, 41(24), 8809–8817. doi: 10.1002/2014GL061855
- 636 Link, F., Reiss, M. C., & Rumpker, G. (2022). An automatized XKS-splitting procedure for large data  
637 sets: Extension package for SplitRacer and application to the USArray. *Computers & Geosciences*,  
638 158, 104961. doi: 10.1016/j.cageo.2021.104961
- 639 Liu, J., Wu, J., Wang, W., Fang, L., & Chang, K. (2020). Seismic anisotropy beneath the eastern margin

- 640 of the Tibetan Plateau from SKS splitting observations. *Tectonophysics*, 785, 228430. doi:  
641 10.1016/j.tecto.2020.228430
- 642 Liu, Q. Y., van Der Hilst, R. D., Li, Y., Yao, H. J., Chen, J. H., Guo, B., Qi, S. H., Wang, J., Huang, H.,  
643 & Li, S. C. (2014). Eastward expansion of the Tibetan Plateau by crustal flow and strain partitioning  
644 across faults. *Nature Geoscience*, 7(5), 361–365. doi: 10.1038/NGEO2130
- 645 Long, M. D., & Becker, T. W. (2010). Mantle dynamics and seismic anisotropy. *Earth and Planetary  
646 Science Letters*, 297(3-4), 341–354.
- 647 Mondal, P., & Long, M. D. (2019). A model space search approach to finite-frequency SKS splitting  
648 intensity tomography in a reduced parameter space. *Geophysical Journal International*, 217, 238-  
649 256. doi: 10.1093/gji/ggz016
- 650 Mondal, P., & Long, M. D. (2020). Strong seismic anisotropy in the deep upper mantle beneath the  
651 Cascadia backarc: Constraints from probabilistic finite-frequency SKS splitting intensity  
652 tomography. *Earth and Planetary Science Letters*, 539, 116172. doi: 10.1016/j.epsl.2020.116172
- 653 Montagner, J.-P., & Nataf, H.-C. (1986). A simple method for inverting the azimuthal anisotropy of  
654 surface waves, *Journal of Geophysical Research*, 91(B1), 511-520.
- 655 Monteiller, V., & Chevrot, S. (2011). High-resolution imaging of the deep anisotropic structure of the San  
656 Andreas Fault system beneath southern California. *Geophysical Journal International*, 186(2), 418-  
657 446. doi: 10.1111/j.1365-246X.2011.05082.x
- 658 Paige, C. C., & Saunders, M. A. (1982). LSQR—an algorithm for sparse linear-equations and sparse least-  
659 squares. *ACM Transactions on Mathematical Software*, 8(1), 43–71.
- 660 Pasyanos, M. E., Masters, T. G., Laske, G., & Ma, Z. (2014). LITHO1. 0: An updated crust and  
661 lithospheric model of the Earth. *Journal of Geophysical Research: Solid Earth*, 119(3), 2153–2173.  
662 doi: 10.1002/2013JB010626
- 663 Quatieri, T. F. (2006). *Discrete-time Speech Signal Processing: Principles and Practice*. Pearson  
664 Education India.
- 665 Royden, L. H., Burchfiel, B. C., & van der Hilst, R. D. (2008). The geological evolution of the Tibetan  
666 Plateau. *Science*, 321(5892), 1054–1058. doi: 10.1126/science.1155371
- 667 Shen, Z.-K., Lü, J., Wang, M., & Bürgmann, R. (2005). Contemporary crustal deformation around the  
668 southeast borderland of the Tibetan Plateau. *Journal of Geophysical Research: Solid Earth*,  
669 110(B11). doi: 10.1029/2004JB003421
- 670 Shi, Y., Gao, Y., Su, Y., & Wang, Q. (2012). Shear-wave splitting beneath Yunnan area of Southwest

- 671 China. *Earthquake Science*, 25(1), 25–34. doi: 10.1007/s11589-012-0828-4
- 672 Sieminski, A., Paulssen, H., Trampert, J., & Tromp, J. (2008). Finite-frequency SKS splitting:  
673 measurement and sensitivity kernels. *Bulletin of the Seismological Society of America*, 98(4), 1797–  
674 1810. doi: 10.1785/0120070297
- 675 Sun, Y., Niu, F., Liu, H., Chen, Y., & Liu, J. (2012). Crustal structure and deformation of the SE Tibetan  
676 plateau revealed by receiver function data. *Earth and Planetary Science Letters*, 349, 186–197. doi:  
677 10.1016/j.epsl.2012.07.007
- 678 Wang, C.-Y., Chan, W. W., & Mooney, W. D. (2003). Three-dimensional velocity structure of crust and  
679 upper mantle in southwestern China and its tectonic implications. *Journal of Geophysical Research:  
680 Solid Earth*, 108(B9). doi: 10.1029/2002JB001973
- 681 Wang, C.-Y., Flesch, L. M., Silver, P. G., Chang, L.-J., & Chan, W. W. (2008). Evidence for mechanically  
682 coupled lithosphere in central Asia and resulting implications. *Geology*, 36(5), 363–366. doi:  
683 10.1130/G24450A.1
- 684 Wang, C.-Y., Lou, H., Silver, P. G., Zhu, L., & Chang, L. (2010). Crustal structure variation along 30°N  
685 in the eastern Tibetan Plateau and its tectonic implications. *Earth and Planetary Science Letters*,  
686 289(3–4), 367–376. doi: 10.1016/j.epsl.2009.11.026
- 687 Wang, M., & Shen, Z.-K. (2020). Present-day crustal deformation of continental China derived from GPS  
688 and its tectonic implications. *Journal of Geophysical Research: Solid Earth*, 125(2),  
689 e2019JB018774. doi: 10.1029/2019JB018774
- 690 Wang, W., Wu, J., Fang, L., Lai, G., & Cai, Y. (2017). Crustal thickness and Poisson's ratio in southwest  
691 China based on data from dense seismic arrays. *Journal of Geophysical Research: Solid Earth*,  
692 122(9), 7219–7235. doi: 10.1002/2017JB013978
- 693 Wei, W., Xu, J., Zhao, D., & Shi, Y. (2012). East Asia mantle tomography: New insight into plate  
694 subduction and intraplate volcanism. *Journal of Asian Earth Sciences*, 60, 88–103. doi:  
695 10.1016/j.jseaes.2012.08.001
- 696 Wei, Z., & Zhao, L. (2019). Lg-Q model and its implication on high-frequency ground motion for  
697 earthquakes in the Sichuan and Yunnan region. *Earth and Planetary Physics*, 3(6), 526–536. doi:  
698 10.26464/epp2019054
- 699 Wei, Z., & Zhao, L. (2022). P-wave velocity structure of the lower crust and uppermost mantle beneath  
700 the Sichuan-Yunnan (China) region. *Seismological Research Letters*, 93(4). doi:  
701 10.1785/0220210357

- 702 Wessel, P., Luis, J., Uieda, L., Scharroo, R., Wobbe, F., Smith, W. H., & Tian, D. (2019). The generic  
703 mapping tools version 6. *Geochemistry, Geophysics, Geosystems*, 20(11), 5556–5564. doi:  
704 10.1029/2019GC008515
- 705 Xu, L., Rondenay, S., & van der Hilst, R. D. (2007). Structure of the crust beneath the southeastern Tibetan  
706 Plateau from teleseismic receiver functions. *Physics of the Earth and Planetary Interiors*, 165(3-4),  
707 176–193. doi: 10.1016/j.pepi.2007.09.002
- 708 Xu, M., Huang, Z., Wang, L., Xu, M., Zhang, Y., Mi, N., Yu, D., & Yuan, X. (2020). Sharp lateral Moho  
709 variations across the SE Tibetan margin and their implications for plateau growth. *Journal of*  
710 *Geophysical Research: Solid Earth*, 125(5), e2019JB018117. doi: 10.1029/2019JB018117
- 711 Xu, Y., Chung, S.-L., Jahn, B.-m., & Wu, G. (2001). Petrologic and geochemical constraints on the  
712 petrogenesis of Permian–Triassic Emeishan flood basalts in southwestern China. *Lithos*, 58, 145–  
713 168.
- 714 Yang, S., Liang, X., Jiang, M., Chen, L., He, Y., Mon, C. T., Hou, G., Thant, M., Sein, K., & Wan, B.  
715 (2022). Slab remnants beneath the Myanmar terrane evidencing double subduction of the Neo-  
716 Tethyan Ocean. *Science Advances*, 8(34), eabo1027. doi: 10.1126/sciadv.abo1027
- 717 Yang, Y., Liang, C., Fang, L., Su, J., & Hua, Q. (2018). A comprehensive analysis on the stress field and  
718 seismic anisotropy in eastern Tibet. *Tectonics*, 37(6), 1648–1657. doi: 10.1029/2018TC005011
- 719 Yang, H., Peng, H., & Hu, J. (2017). The lithospheric structure beneath southeast Tibet revealed by P and  
720 S receiver functions. *Journal of Asian Earth Sciences*, 138, 62–71.  
721 <https://doi.org/10.1016/j.jseaes.2017.02.001>
- 722 Yang, Y., Yao, H., Wu, H., Zhang, P., & Wang, M. (2019). A new crustal shear-velocity model in  
723 Southwest China from joint seismological inversion and its implications for regional crustal  
724 dynamics. *Geophysical Journal International*, 220, 1379–1393. <https://doi.org/10.1093/gji/ggz514>
- 725 Yang, Y., Zheng, Y., Chen, J., Zhou, S., Celyan, S., Sandvol, E., Tilmann, F., Priestley, K., Hearn, T. M.,  
726 Ni, J. F., Brown, L. D., & Ritzwoller, M. H. (2010). Rayleigh wave phase velocity maps of Tibet and  
727 the surrounding regions from ambient seismic noise tomography. *Geochemistry, Geophysics,*  
728 *Geosystems*, 11(8). doi:10.1029/2010GC003119
- 729 Yao, H. J., van der Hilst, R. D., & Montagner, J. P. (2010). Heterogeneity and anisotropy of the lithosphere  
730 of SE Tibet from surface wave array tomography. *Journal of Geophysical Research: Solid Earth*,  
731 115. doi: 10.1029/2009JB007142
- 732 Yin, A., & Harrison, T. M. (2000). Geologic evolution of the Himalayan-Tibetan orogen. *Annual Review*

- 733 *of Earth and Planetary Sciences*, 28(1), 211–280.
- 734 Zhang, F., Wu, Q., Li, Y., Zhang, R., Sun, L., Pan, J., & Ding, Z. (2018). Seismic tomography of eastern  
735 Tibet: Implications for the Tibetan Plateau growth. *Tectonics*, 37(9), 2833–2847. doi:  
736 10.1029/2018TC004977
- 737 Zhang, G. W., Guo, A. L., Wang, Y. J., Li, S. Z., Dong, Y. P., Liu, S. F., He, D. F., Cheng, S. Y., Lu, R.  
738 K., & Yao, A. P. (2013). Tectonics of South China Continent and its implications. *Science China  
739 Earth Sciences*, 56, 1804–1828. doi: 10.1007/s11430-013-4679-1
- 740 Zhang, P., Deng, Q., Zhang, G., Ma, J., Gan, W., Min, W., Mao, F., & Wang, Q. (2003). Active tectonic  
741 blocks and strong earthquakes in the continent of China. *Science China Earth Sciences*, 46(2), 13–  
742 24. doi: 10.1360/03dz0002
- 743 Zhang, P.-Z. (2013). A review on active tectonics and deep crustal processes of the western Sichuan  
744 region, eastern margin of the Tibetan Plateau. *Tectonophysics*, 584, 7–22. doi:  
745 10.1016/j.tecto.2012.02.021
- 746 Zhang, Z., Wang, Y., Chen, Y., Houseman, G. A., Tian, X., Wang, E., & Teng, J. (2009). Crustal structure  
747 across Longmenshan fault belt from passive source seismic profiling. *Geophysical Research Letters*,  
748 36(17). doi: 10.1029/2009GL039580
- 749 Zhang, Z., Yao, H., & Yang, Y. (2020). Shear wave velocity structure of the crust and upper mantle in  
750 Southeastern Tibet and its geodynamic implications. *Science China Earth Sciences*, 63, 1278–1293.  
751 <https://doi.org/10.1007/s11430-020-9625-3>
- 752 Zhang, Z., Feng, J., & Yao, H. (2023). 3-D azimuthal anisotropy structure reveals different deformation  
753 modes of the crust and upper mantle in the southeastern Tibetan Plateau. *Frontiers in Earth Science*,  
754 11, 1095609. doi: 10.3389/feart.2023.1095609
- 755 Zhao, G., Unsworth, M. J., Zhan, Y., Wang, L., Chen, X., Jones, A. G., Tang, J., Xiao, Q., Wang, J., Cai,  
756 J., Li, T., Wang, Y., & Zhang, J. (2012). Crustal structure and rheology of the Longmenshan and  
757 Wenchuan Mw 7.9 earthquake epicentral area from magnetotelluric data. *Geology*, 40(12), 1139–  
758 1142. doi: 10.1130/G33703.1
- 759 Zhao, L., & Chevrot, S. (2011). An efficient and flexible approach to the calculation of three-dimensional  
760 full-wave fréchet kernels for seismic tomography—II. Numerical results. *Geophysical Journal  
761 International*, 185(2), 939–954. doi: 10.1111/j.1365-246X.2011.04984.x
- 762 Zhao, L., Jordan, T. H., & Chapman, C. H. (2000). Three-dimensional Fréchet differential kernels for  
763 seismic delay times, *Geophysical Journal International*, 141(3), 558–576. doi: 10.1046/j.1365-

764 246x.2000.00085.x

765 Zhao, L. F., Xie, X. B., He, J. K., Tian, X., & Yao, Z. X. (2013). Crustal flow pattern beneath the Tibetan  
766 Plateau constrained by regional Lg-wave Q tomography. *Earth and Planetary Science Letters*, 383,  
767 113–122. doi: 10.1016/j.epsl.2013.09.038.

768

769 **Figure Captions**

770 **Figure 1.** Map of the tectonic environment of SE margin of Tibetan Plateau with seismic stations (green-  
 771 filled triangles) and epicenters (red open circles) of earthquakes of magnitude 5 and above from 2000 to  
 772 2022. The blue triangle marks the station WXT for which SKS waveforms, splitting intensities and  
 773 sensitivity kernels are shown in Figures 4, 5 and 7, respectively. Major active faults are shown by thick  
 774 black lines with abbreviated names in black, including LMSF: Longmenshan Fault; XSHF: Xianshuihe  
 775 Fault; JSJF: Jinshajiang Fault; LCJF: Lancangjiang Fault; LJ-XJHF: Lijiang-Xiaojinhe Fault; ANH-  
 776 ZMHF: Anninghe-Zemuhe Fault; XJF: Xiaojiang Fault; and RRF: Red River Fault. Major active tectonic  
 777 blocks are indicated by abbreviated texts in blue, including SGT: Songpan-Ganzi Terrane; SCB: Sichuan  
 778 Basin; QTB: Qiangtang Block; SYRB: Sichuan-Yunnan Rhombic Block; YTC: Yangtze Craton; and ICB:  
 779 Indo-China Block. EHS stands for the Eastern Himalaya Syntax. Blue cross arrows show the surface strain  
 780 rate derived from GPS observation (Wang & Shen, 2020). Background color shows the topography. The  
 781 black box in the inset map indicates the location of the main figure.

782 **Figure 2.** Lithosphere thickness map. The global model LITHO1.0 (Pasyanos et al., 2014) is shown for  
 783 the region north of 27°N, whereas to the south the regional model of Yang et al. (2017) is depicted. Names  
 784 of major faults and tectonic blocks are the same as in Figure 1.

785 **Figure 3.** Distribution of 470 teleseismic events used for SKS splitting intensity inversion in this study.  
 786 Events of magnitudes  $M_w 5.5$  and greater in the epicentral distance range of  $90^\circ$ – $130^\circ$  during 2009–2020  
 787 are selected. The red box in the center indicates the study area.

788 **Figure 4.** An example of SKS window selection using SplitRacer. (a) and (b) show normalized radial and  
 789 transverse records, respectively, around the SKS arrival at station WXT (blue triangle in Figure 1) from  
 790 the 24 June 2019 earthquake in New Zealand with a back azimuth of  $122^\circ$ . The green lines mark the  
 791 theoretical SKS and SKKS arrival times corresponding to the event of interest. Red vertical lines mark  
 792 the start and end times of the final window used for SI measurement. (c) Summed spectral power of the  
 793 spectrogram of the radial and transverse records in (a) and (b). The red horizontal line marks the frequency  
 794 of maximum spectral power, and the red dashed lines show the frequency bounds of more than 80% of  
 795 the maximum. The green vertical lines mark the time window in which the summed spectral power is  
 796 more than 50% of the maximum. (d) Summed spectral power over all frequencies. The green vertical lines  
 797 mark the time window in which the summed spectral energy is more than 50% of the maximum. (e)  
 798 STA/LTA ratio of the radial-component record used as quality check. The blue vertical line denotes the  
 799 time when the STA/LTA ratio reaches its peak within the window determined in (d). The red horizontal

800 line is the acceptance threshold of 2.1 (Link et al., 2022).

801 **Figure 5.** Variations of measured SI with event back azimuth for station WXT (blue triangle in Figure 1)  
 802 before (a) and after (b) removal of SI outliers. The vertical error bars show two standard deviations ( $2\sigma_i$ )  
 803 of individual measurements. The dashed lines represent the sinusoidal curves that best fit the  
 804 measurements. According to Eq. (2), the conventional SKS splitting parameters for this station are:  $\Delta t =$   
 805  $1.08$  s and  $\theta = 109.14^\circ$ .

806 **Figure 6.** Black line segments show the conventional SKS fast-direction azimuths and delay times at all  
 807 station obtained from the SI measurements according to Eq. (2). Red line segments are fast-direction  
 808 azimuths and delay times derived from Eq. (2) based on the model-predicted SIs obtained by integrating  
 809 the sensitivity kernels (see Figure 7) with the anisotropy model in Figure 12 according to Eq. (4). Names  
 810 of major faults and tectonic blocks are the same as in Figure 1.

811 **Figure 7.** Examples of the sensitivity kernels of the SI to shear wave anisotropy parameters  $\gamma_c$  (a) and  $\gamma_s$   
 812 (b) shown in mapviews for the 146-km depth and in profiles (insets) along source-receiver path AA' for  
 813 station WXT (blue triangle in Figure 1). The SKS wave is from the 24 June 2019 event in New Zealand  
 814 with a back azimuth of  $122^\circ$ , and the waveforms are shown in Figure 4.

815 **Figure 8.** Resolution tests for the azimuth of symmetry axis using  $1^\circ \times 1^\circ$  checkerboard. (Top-left) The  
 816 input model has horizontally alternating azimuthal angles of fast axes  $\phi_f = 90^\circ$  and  $\phi_f = 45^\circ$  shown by  
 817 both the color and the directions of the line segments, and a fixed anisotropy strength  $\gamma = 4\%$  represented  
 818 by the lengths of the line segments. The two white dashed lines show the locations of profiles NS and N'S'  
 819 in Figure 11. The other panels show the recovered models at a depth of 55 km for different damping  
 820 factors  $\lambda$ . We choose  $\lambda = 4$  as the optimal value for the damping factor (top-right panel). Red triangles  
 821 show locations of stations used.

822 **Figure 9.** Resolution test using  $1^\circ \times 1^\circ$  checkerboard. (Top-left) The input model has horizontally  
 823 alternating anisotropy strengths shown by the colors representing perturbations of  $\delta\gamma = \pm 3\%$  relative to  
 824 a background anisotropy strength of  $\gamma = 4\%$ , and a fixed azimuthal angle of symmetry axis  $\phi_f = 22.5^\circ$ .  
 825 The other panels show the recovered models at a depth of 55 km for different damping factors  $\lambda$ . We  
 826 choose  $\lambda = 4$  as the optimal value for the damping factor (top-right panel).

827 **Figure 10.** Resolution test using  $1^\circ \times 1^\circ$  checkerboard with damping factor  $\lambda = 4$ . (Upper panels)  
 828 Recovered model at the depths of 99 km, 165 km, 208 km and 274 km for an input model having  
 829 horizontally alternating azimuthal angles of fast axes  $\phi_f = 90^\circ$  and  $\phi_f = 45^\circ$  with a fixed anisotropy  
 830 strength  $\gamma = 4\%$ . The input model and the recovered model at 55-km depth are shown in Figure 8. (Lower

831 panels) Recovered model at the depths of 99 km, 165 km, 208 km and 274 km for an input model with  
 832 horizontally alternating anisotropy strengths of  $\gamma = 1\%$  and  $\gamma = 7\%$  (perturbations of  $\delta\gamma = \pm 3\%$   
 833 relative to a background anisotropy strength of  $\gamma = 4\%$ ) with a fixed azimuthal angle of symmetry axis  
 834  $\phi_f = 22.5^\circ$ . The input model and the recovered model at 55-km depth are shown in Figure 9.

835 **Figure 11.** Resolution tests for an input model with 4 layers of alternating azimuthal angles of symmetry  
 836 axes  $\phi_f = 45^\circ$  and  $\phi_f = 135^\circ$  but a fixed anisotropy strength of  $\gamma = 4\%$ . Shown here are the input model  
 837 (top-left panel) and recovered models for different damping factors  $\lambda$  along the north-south cross-section  
 838 NS through the middle of the study region (see top-left panel in Figure 8). The optimal damping is  $\lambda = 4$   
 839 (middle-left panel).

840 **Figure 12.** Three-dimensional anisotropic model for the SE margin of Tibetan Plateau at 55 km, 99 km,  
 841 165 km, 208 km and 274 km depths. The anisotropy strength and the azimuth of the fast axes are shown  
 842 by the background color and the black line segments, respectively. The lengths of the line segments are  
 843 proportional to the anisotropy strength. The black and green arrows denote the absolute plate motion  
 844 (APM) of the Eurasian and Indian plates, respectively, according to the model NNR-MORVEL56 (Argus  
 845 et al., 2011). The white dashed lines show locations of the profiles shown in Figure 13. Names of major  
 846 faults and tectonic blocks are the same as in Figure 1. Blue triangles show locations of stations used.  
 847 Regions in which the recovery errors are above 20% are mask out. The recovery error is defined by  $E =$   
 848  $(|\phi_f - \tilde{\phi}_f|/90^\circ) \times 100\%$ , where  $\tilde{\phi}_f$  and  $\phi_f$  are the input and recovered azimuthal angles in the  
 849 resolution tests in Figures 8 and 10.

850 **Figure 13.** Vertical profiles of the azimuths of fast axis in our 3D anisotropy model along (a) 26°N latitude,  
 851 (b) 32°N latitude, (c) 100°E longitude and (d) 104°E longitude. The azimuths of the fast axis are shown by  
 852 the background color. Note that red ( $\sim 0^\circ$ ) and blue ( $\sim 180^\circ$ ) colors both indicate nearly N-S fast axis,  
 853 whereas yellow color indicates nearly E-W fast axis. Moho and lithosphere-asthenosphere boundary (LAB)  
 854 are depicted by thick black and white lines, respectively. Names of major faults and tectonic blocks are  
 855 the same as in Figure 1.

856 **Figure 14.** Result of the recovery test. The recovered and input anisotropic models are compared at five  
 857 depths marked at the bottom-right corner in each panel. Black and red line segments denote the directions  
 858 of fast axes in the input and recovered models, respectively, and their lengths indicates the anisotropy  
 859 strength. Names of major faults and tectonic blocks are the same as in Figure 1. Blue triangles show  
 860 locations of stations used.

861 **Figure 15.** Comparison of SKS splitting times and fast axis directions predicted by our anisotropy model

862 (Figure 12) with previous studies. Black line segments are results from the present study, whereas blue and red  
863 line segments show results from Chang et al. (2015) and Liu et al. (2020), respectively. Blue and red ellipses  
864 highlight stations where there are large discrepancies in splitting parameters between this study and Liu et al.  
865 (2020) and Chang et al. (2015), respectively. Names of major faults and tectonic blocks are the same as in  
866 Figure 1.

2 **Supporting Information for**

3 **Upper-mantle anisotropy in the southeastern margin of Tibetan Plateau revealed by**  
4 **fullwave SKS splitting intensity tomography**

5 Yi Lin<sup>1,2</sup> and Li Zhao<sup>1,3\*</sup>

6 <sup>1</sup> *School of Earth and Space Sciences, Peking University, Beijing 100871, China.*

7 <sup>2</sup> *Key Laboratory of Earth Exploration and Information Techniques of the China Ministry of*  
8 *Education, Chengdu University of Technology, Chengdu 610059, China.*

9 <sup>3</sup> *Hebei Hongshan National Geophysical Observatory, Peking University, Beijing 100871, China.*

10 \* Corresponding author: Li Zhao (lizhaopku@pku.edu.cn)

11  
12 **This Supporting Information contains 14 Supplementary Figures S1-S14.**

13 **Figure S1:** Resolution test results at different depths for 45° variation in the azimuth of  
14 symmetry axis using 1° x 1° checkerboard and different damping factors.

15 **Figure S2:** Resolution test results at different depths for 45° variation in the azimuth of  
16 symmetry axis using 1.5° x 1.5° checkerboard and different damping factors.

17 **Figure S3:** Resolution test results at different depths for 90° variation in the azimuth of  
18 symmetry axis using 1° x 1° checkerboard and different damping factors.

19 **Figure S4:** Resolution test results at different depths for 90° variation in the azimuth of  
20 symmetry axis using 1.5° x 1.5° checkerboard and different damping factors.

21 **Figure S5:** Resolution test results at different depths for anisotropy strength using 1° x 1°  
22 checkerboard and different damping factors.

23 **Figure S6:** Resolution test results at different depths for anisotropy strength using 1.5° x  
24 1.5° checkerboard and different damping factors.

25 **Figure S7:** Resolution tests for the azimuth of symmetry axis using a 2-layer input model  
26 and different damping factors.

27 **Figure S8:** Resolution tests for anisotropy strength using a 2-layer input model and  
28 different damping factors.

29 **Figure S9:** Resolution tests for the azimuth of symmetry axis using a 4-layer input model  
30 and different damping factors.

31 **Figure S10:** Resolution tests for anisotropy strength using a 4-layer input model and  
32 different damping factors.

33 **Figure S11.** Resolution tests result at 55-km depth for the azimuth of symmetry axis using  
34  $1^\circ \times 1^\circ$  checkerboard with a substantially increased standard deviation (0.3 s) of the  
35 Gaussian noise.

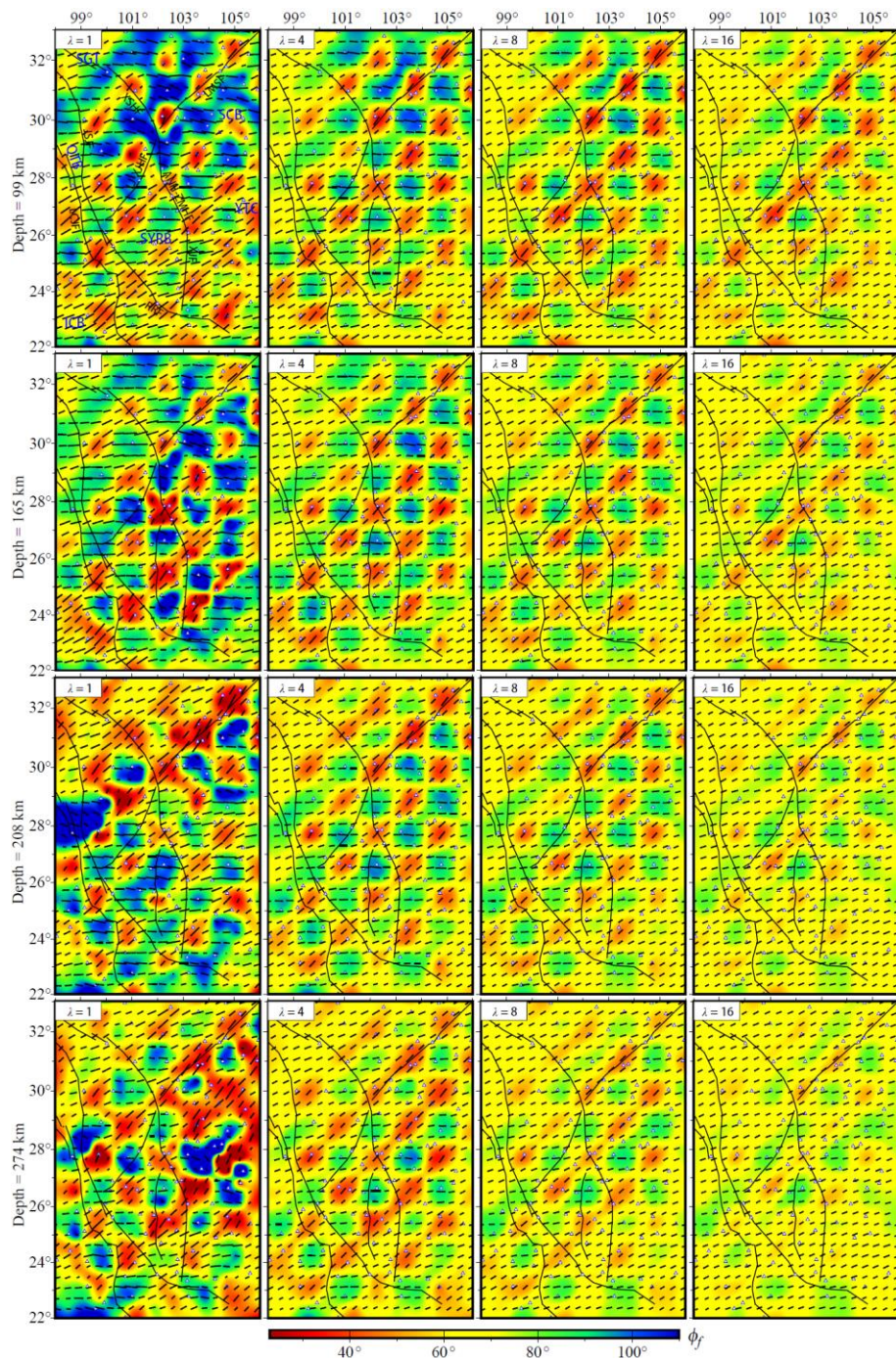
36 **Figure S12.** Result at different depth for the same resolution test as Figure S11.

37 **Figure S13.** Resolution tests result at 55-km depth for anisotropy strength using  $1^\circ \times 1^\circ$   
38 checkerboard with a substantially increased standard deviation (0.3 s) of the Gaussian noise.

39 **Figure S14.** Result at different depth for the same resolution test as Figure S13.

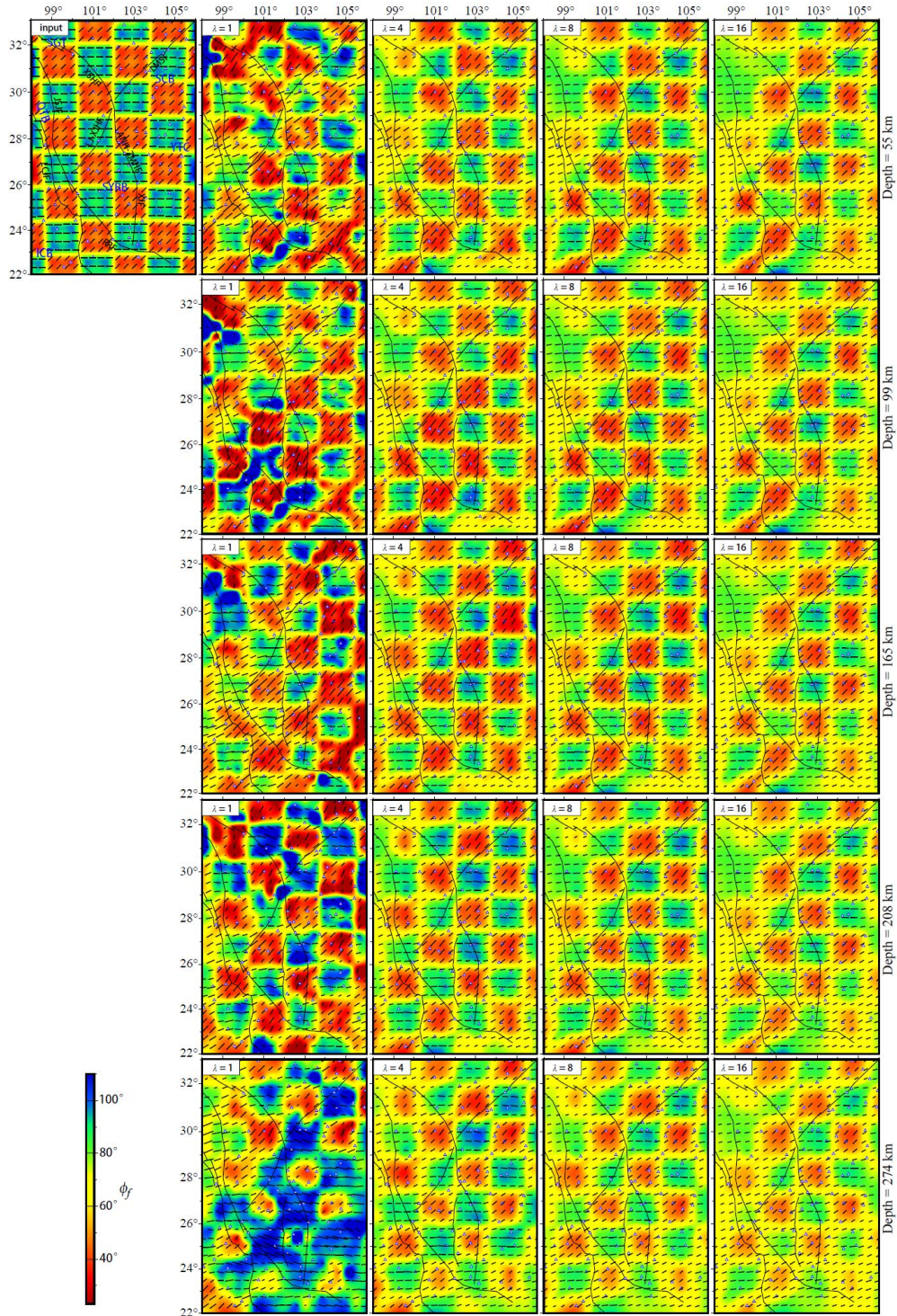
40

41 **Supplementary Figures**



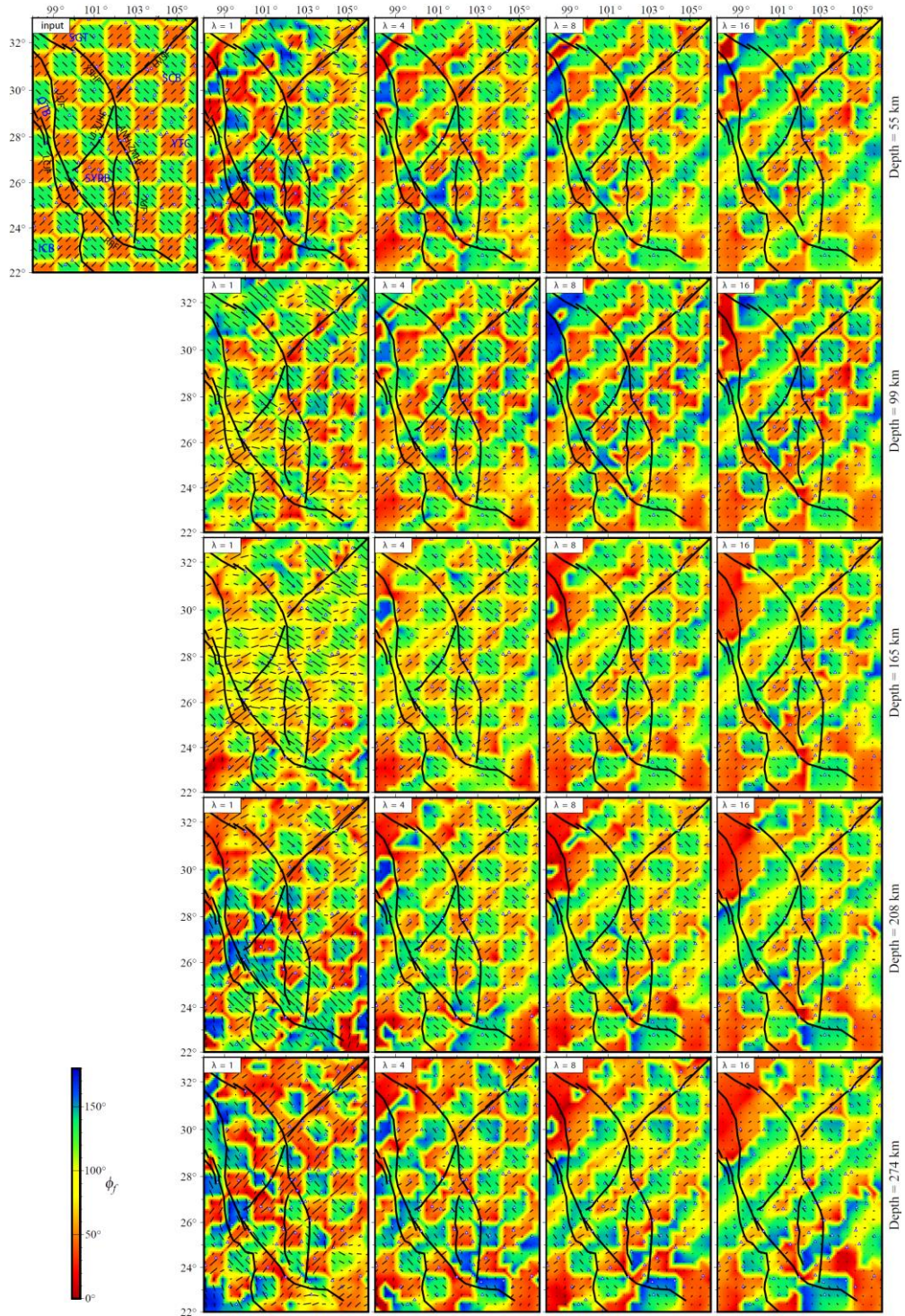
42

43 **Figure S1.** Resolution tests for the azimuth of symmetry axis using  $1^\circ \times 1^\circ$  checkerboard.  
 44 The input model (top-left panel of Figure 8) has horizontally alternating azimuthal angles  
 45 of fast axes  $\phi_f = 90^\circ$  and  $\phi_f = 45^\circ$  shown by both the color and the directions of the line  
 46 segments, and a fixed anisotropy strength  $\gamma = 4\%$  represented by the lengths of the line  
 47 segments. Shown here are recovered models using different damping factors (left to right)  
 48 at different depths (top to bottom).



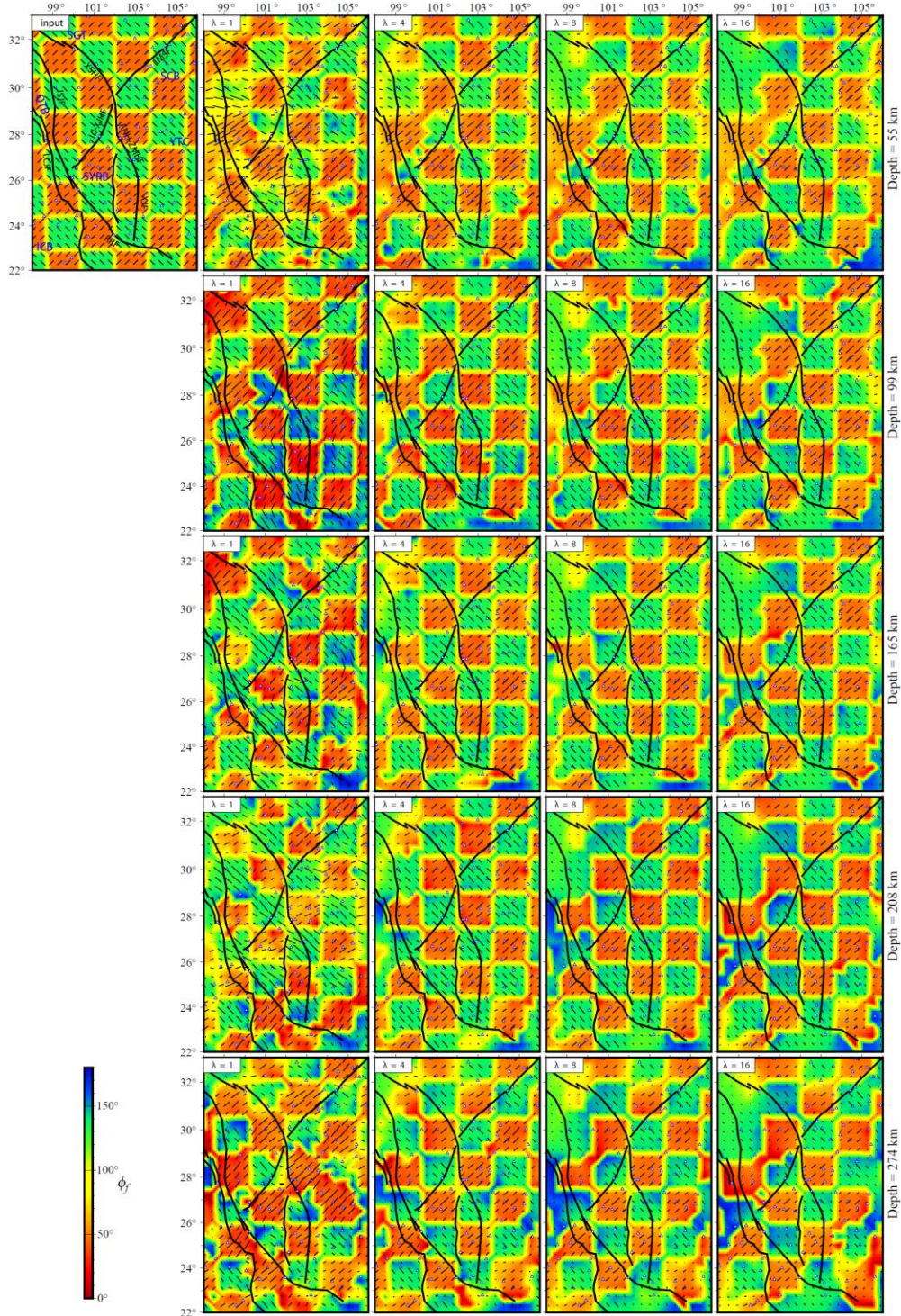
49

50 **Figure S2.** Resolution tests for the azimuth of symmetry axis using  $1.5^\circ \times 1.5^\circ$   
 51 checkerboard. The input model (top-left panel) has horizontally alternating azimuthal  
 52 angles of fast axes  $\phi_f = 90^\circ$  and  $\phi_f = 45^\circ$  shown by both the color and the directions of  
 53 the line segments, and a fixed anisotropy strength  $\gamma = 4\%$  represented by the lengths of  
 54 the line segments. The rest of the panels show recovered models using different damping  
 55 factors (left to right) at different depths (top to bottom).



56

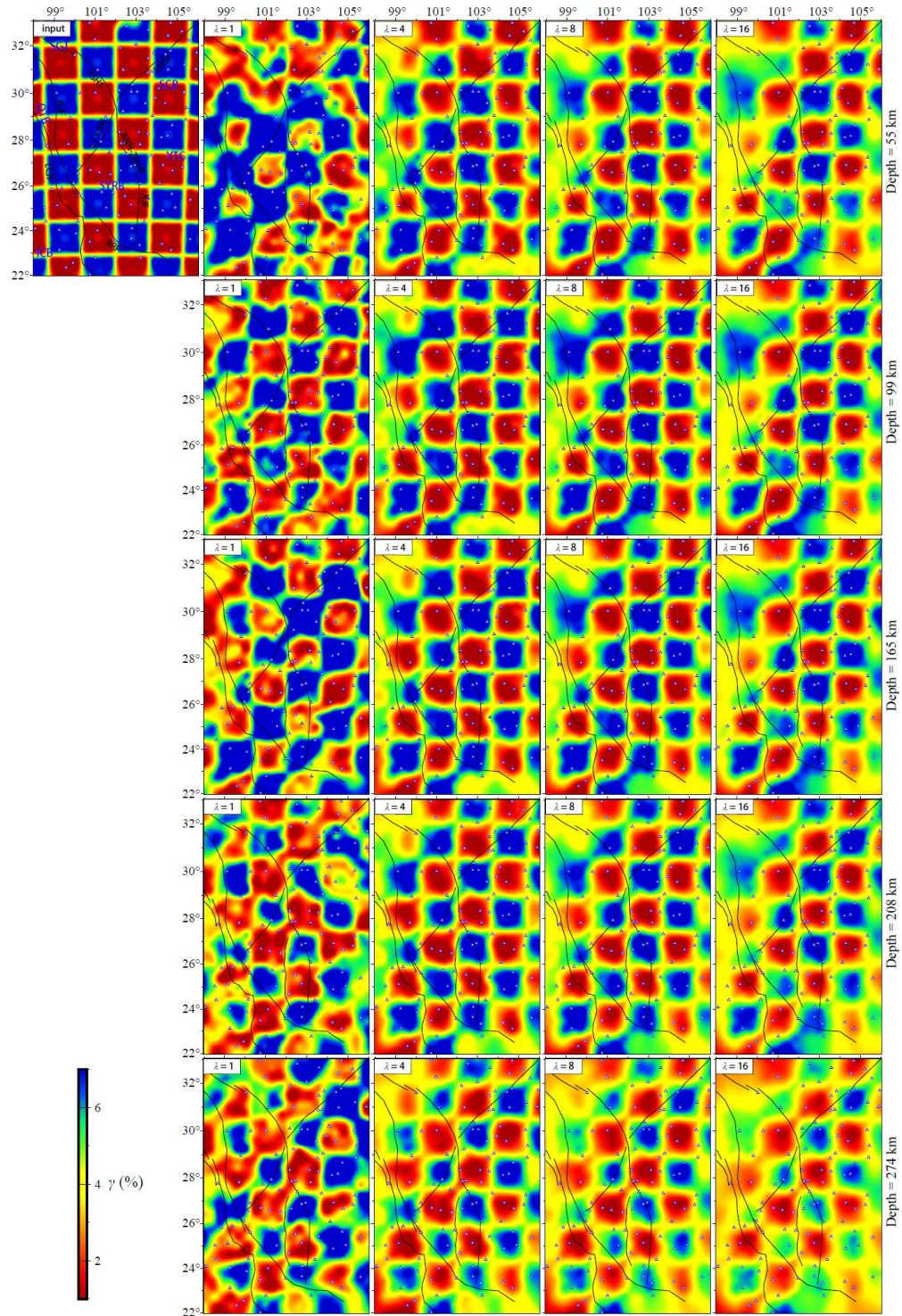
57 **Figure S3.** Resolution tests for the azimuth of symmetry axis using  $1^\circ \times 1^\circ$  checkerboard.  
 58 The input model (top-left panel) has horizontally alternating azimuthal angles of fast axes  
 59  $\phi_f = 45^\circ$  and  $\phi_f = 135^\circ$  shown by both the color and the directions of the line segments,  
 60 and a fixed anisotropy strength  $\gamma = 4\%$  represented by the lengths of the line segments.  
 61 Shown here are recovered models using different damping factors (left to right) at different  
 62 depths (top to bottom).



63

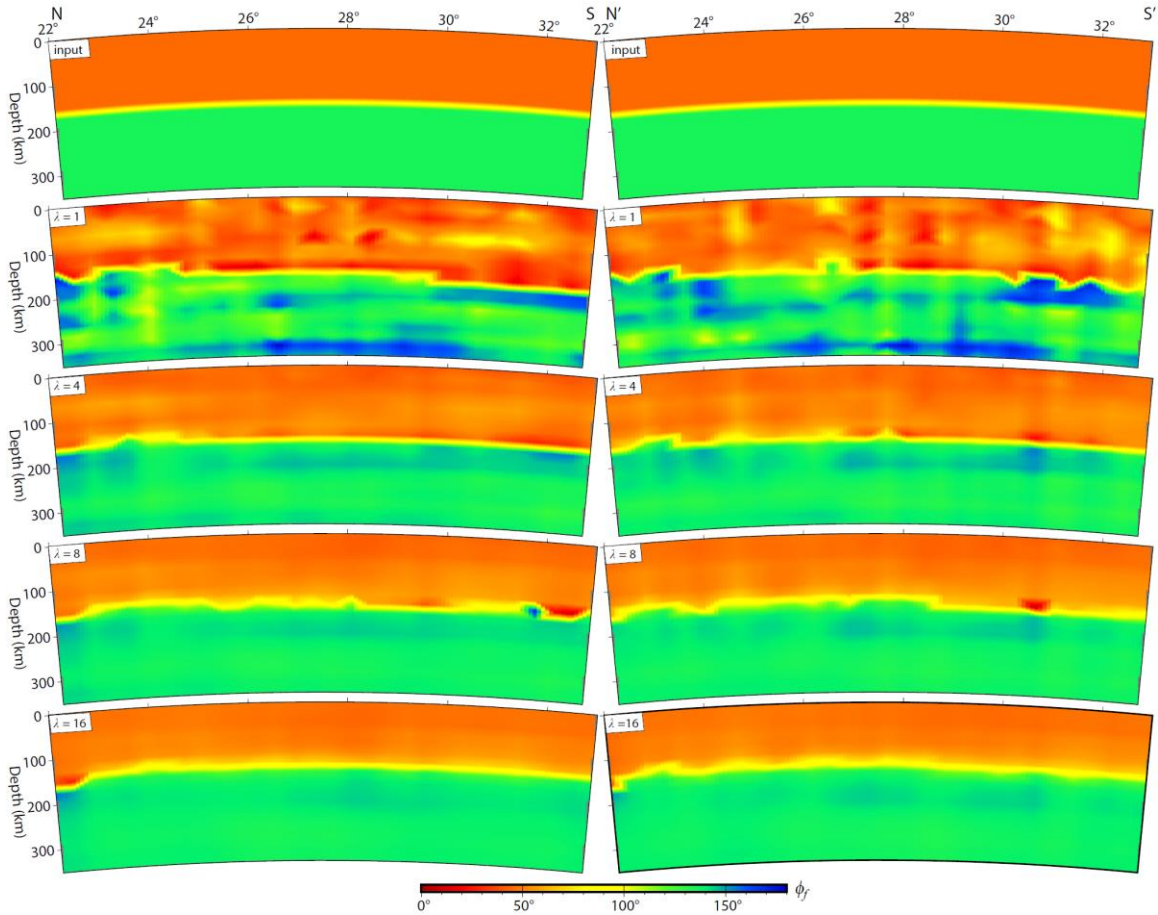
64 **Figure S4.** Resolution tests for the azimuth of symmetry axis using  $1.5^\circ \times 1.5^\circ$   
 65 checkerboard. The input model (top-left panel) has horizontally alternating azimuthal  
 66 angles of fast axes  $\phi_f = 45^\circ$  and  $\phi_f = 135^\circ$  shown by both the color and the directions of  
 67 the line segments, and a fixed anisotropy strength  $\gamma = 4\%$  represented by the lengths of  
 68 the line segments. The rest of the panels show recovered models using different damping  
 69 factors (left to right) at different depths (top to bottom).





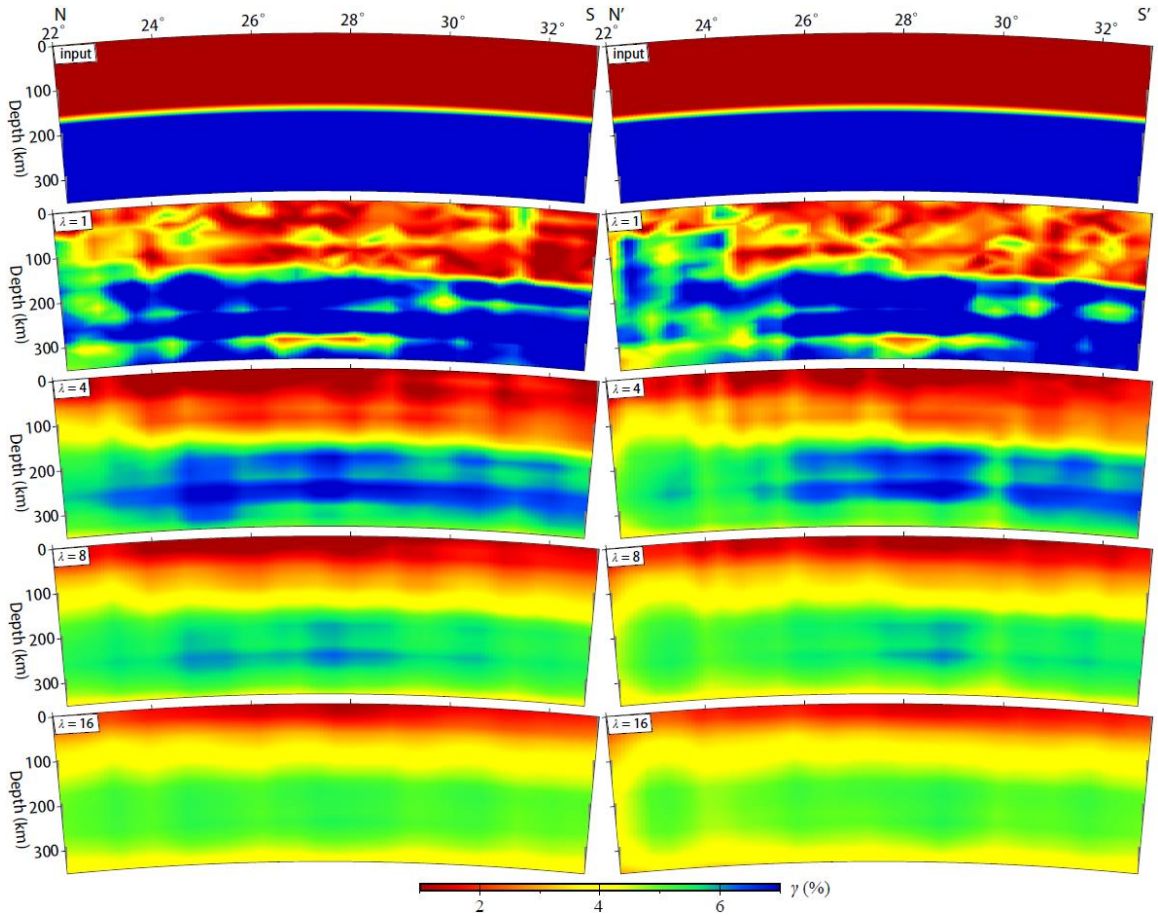
78

79 **Figure S6.** Resolution tests for anisotropy strength using  $1.5^\circ \times 1.5^\circ$  checkerboard. The  
 80 input model (top-left panel) has horizontally alternating anisotropy strengths shown by the  
 81 colors representing perturbations of  $\delta\gamma = \pm 0.03$  relative to a background anisotropy  
 82 strength of  $\gamma = 0.04$  and a fixed azimuthal angle of symmetry axis  $\phi_f = 22.5^\circ$ . The rest  
 83 of the panels show recovered models using different damping factors (left to right) at  
 84 different depths (top to bottom).



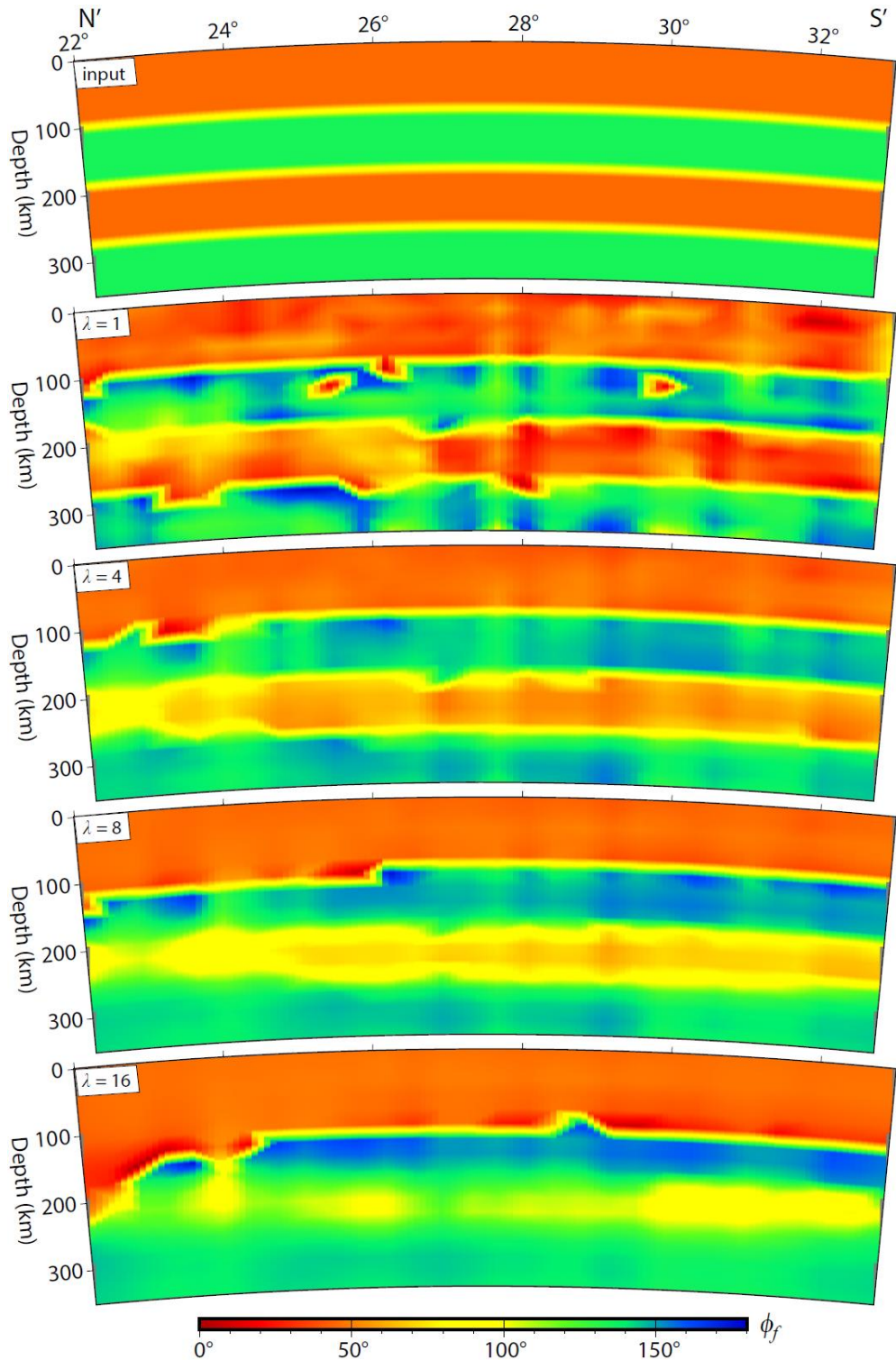
85

86 **Figure S7.** Resolution tests for an input model with 2 layers of different azimuthal angles  
 87 of symmetry axes  $\phi_f = 45^\circ$  and  $\phi_f = 135^\circ$  but a fixed anisotropy strength of  $\gamma = 4\%$ .  
 88 Shown here are the input models (top two panels) along the NS and N'S' cross-sections  
 89 (see top-left panel in Figure 8 for the locations of the cross-sections) and recovered models  
 90 for different damping factors  $\lambda$  (lower panels).



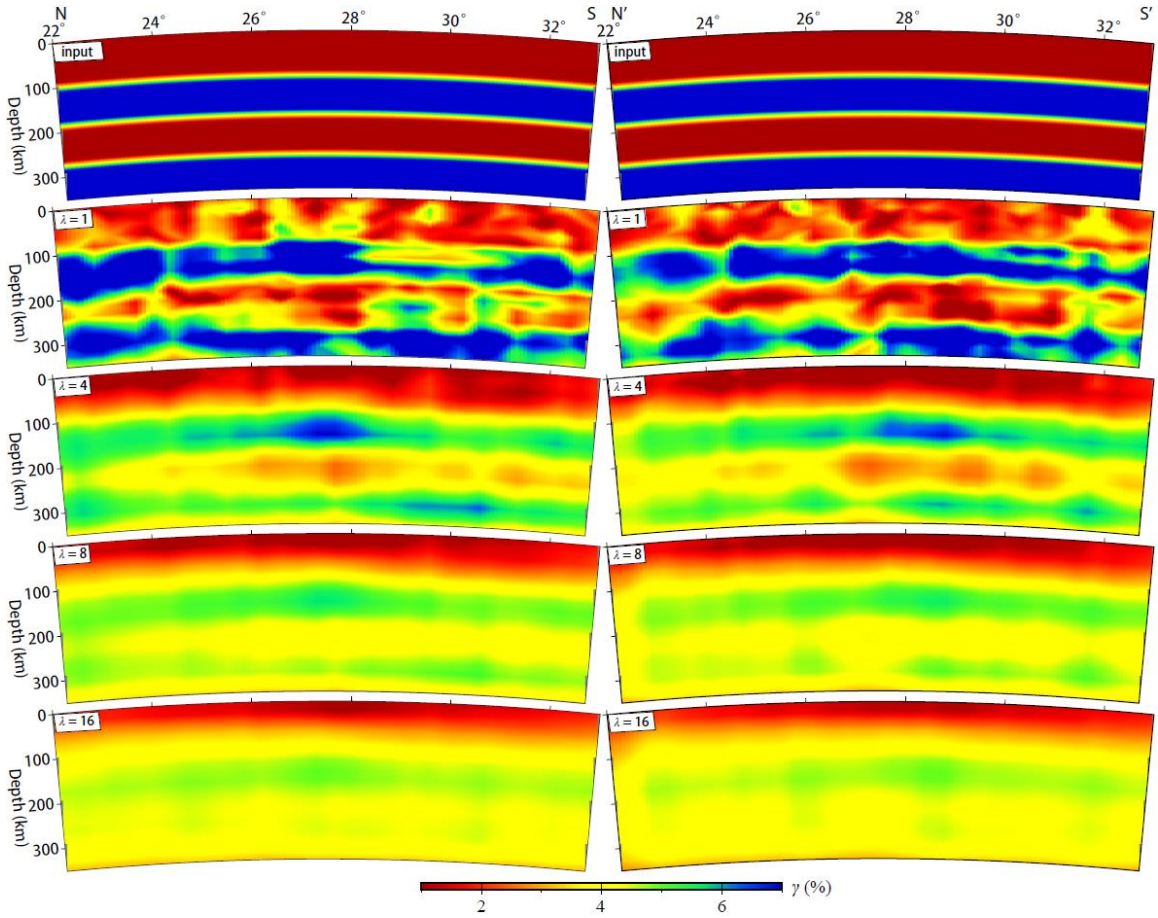
91

92 **Figure S8.** Resolution tests for an input model with 2 layers of different anisotropy  
 93 strengths shown by the colors representing perturbations of  $\delta\gamma = \pm 0.03$  relative to a  
 94 background anisotropy strength of  $\gamma = 0.04$  and a fixed azimuthal angle of symmetry axis  
 95  $\phi_f = 22.5^\circ$ . Shown here are the input models (top two panels) along the NS and N'S'  
 96 cross-sections (see top-left panel in Figure 8 for the locations of the cross-sections) and recovered  
 97 models for different damping factors  $\lambda$  (lower panels).



98

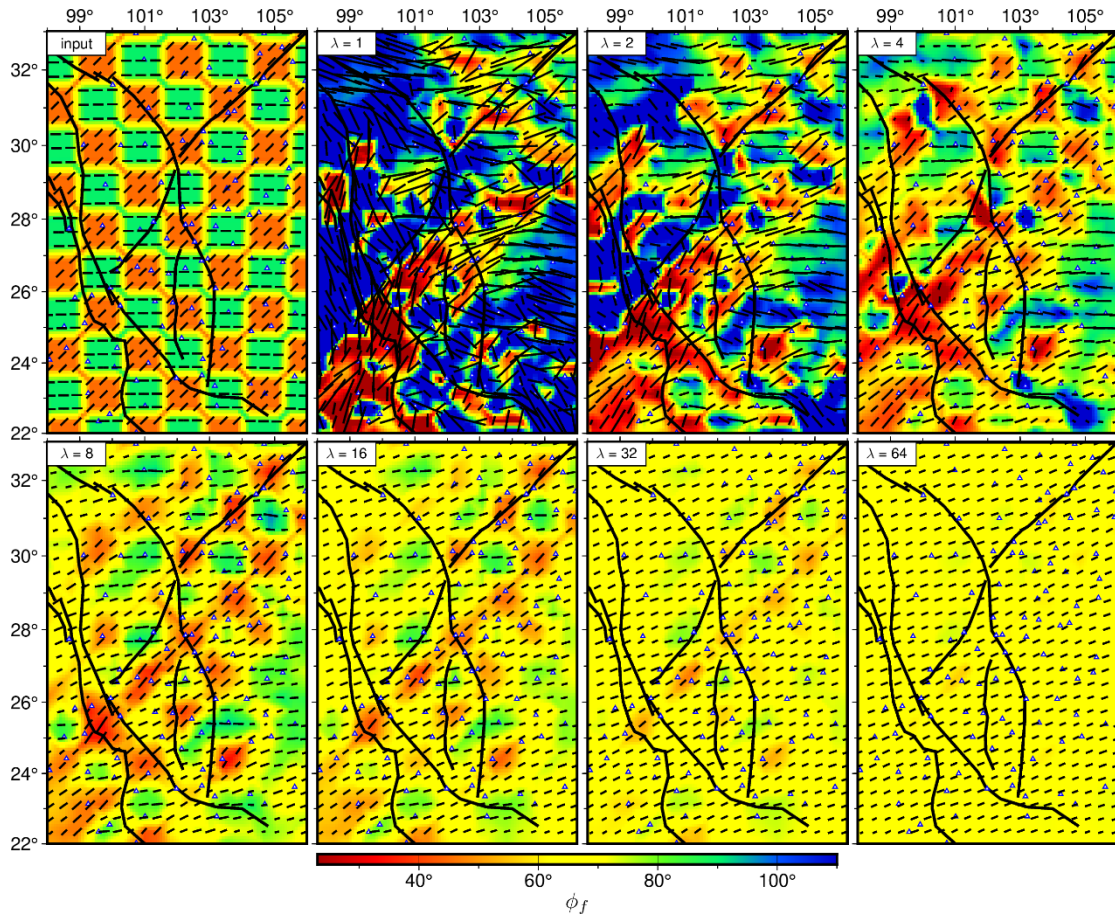
99 **Figure S9.** Resolution tests for an input model with 4 layers of alternating azimuthal angles  
 100 of symmetry axes  $\phi_f = 45^\circ$  and  $\phi_f = 135^\circ$  but a fixed anisotropy strength of  $\gamma = 4\%$ .  
 101 Shown here are the input model (top panel) along the N'S' cross-section (see top-left panel  
 102 in Figure 8 for the location of the cross-section) and recovered models for different  
 103 damping factors  $\lambda$  (lower panels).



104

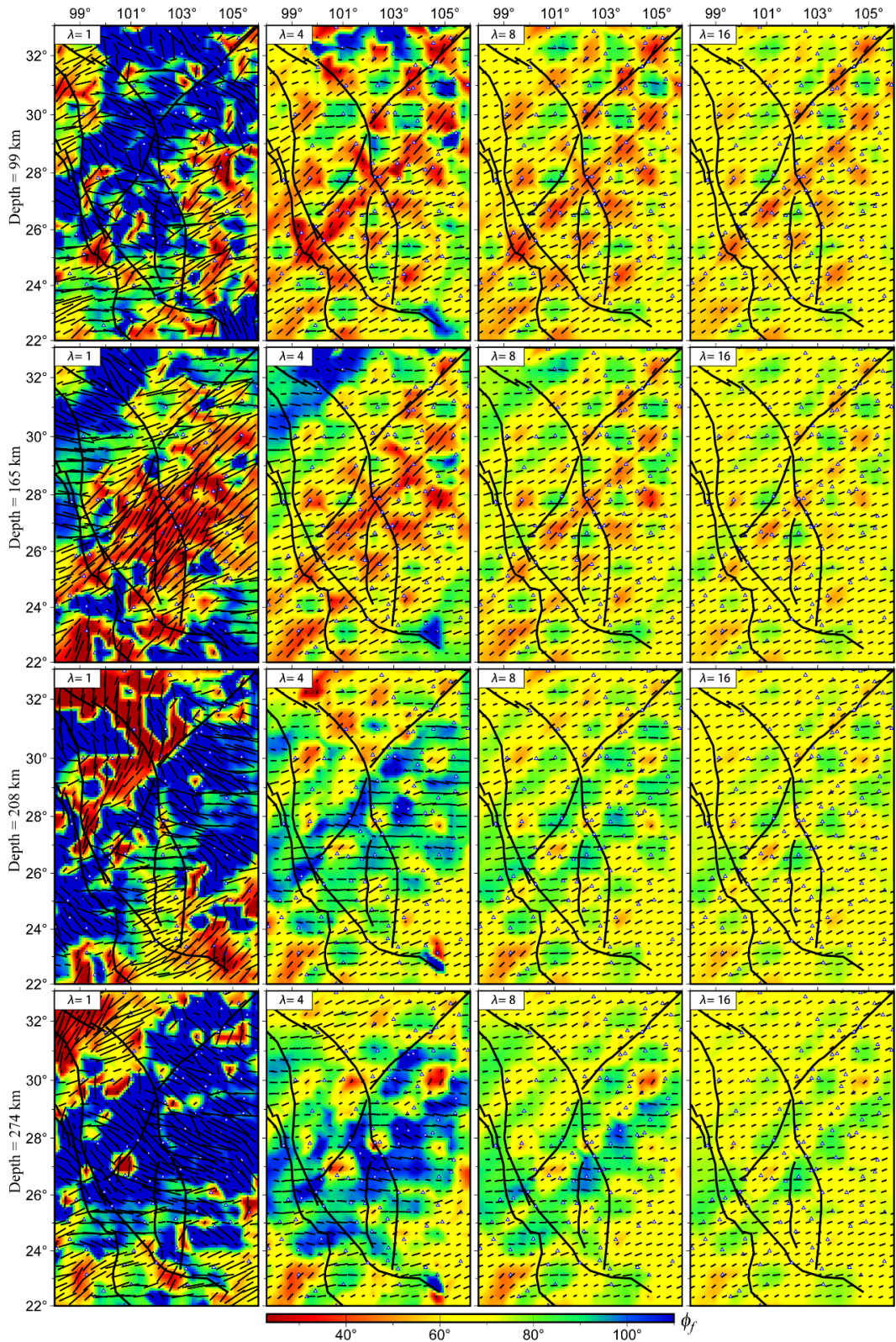
105 **Figure S10.** Resolution tests for an input model with 4 layers of alternating anisotropy  
 106 strengths shown by the colors representing perturbations of  $\delta\gamma = \pm 0.03$  relative to a  
 107 background anisotropy strength of  $\gamma = 0.04$  and a fixed azimuthal angle of symmetry axis  
 108  $\phi_f = 22.5^\circ$ . Shown here are the input models (top two panels) along the NS and N'S'  
 109 cross-sections (see top-left panel in Figure 8 for the locations of the cross-sections) and recovered  
 110 models for different damping factors  $\lambda$  (lower panels).

111



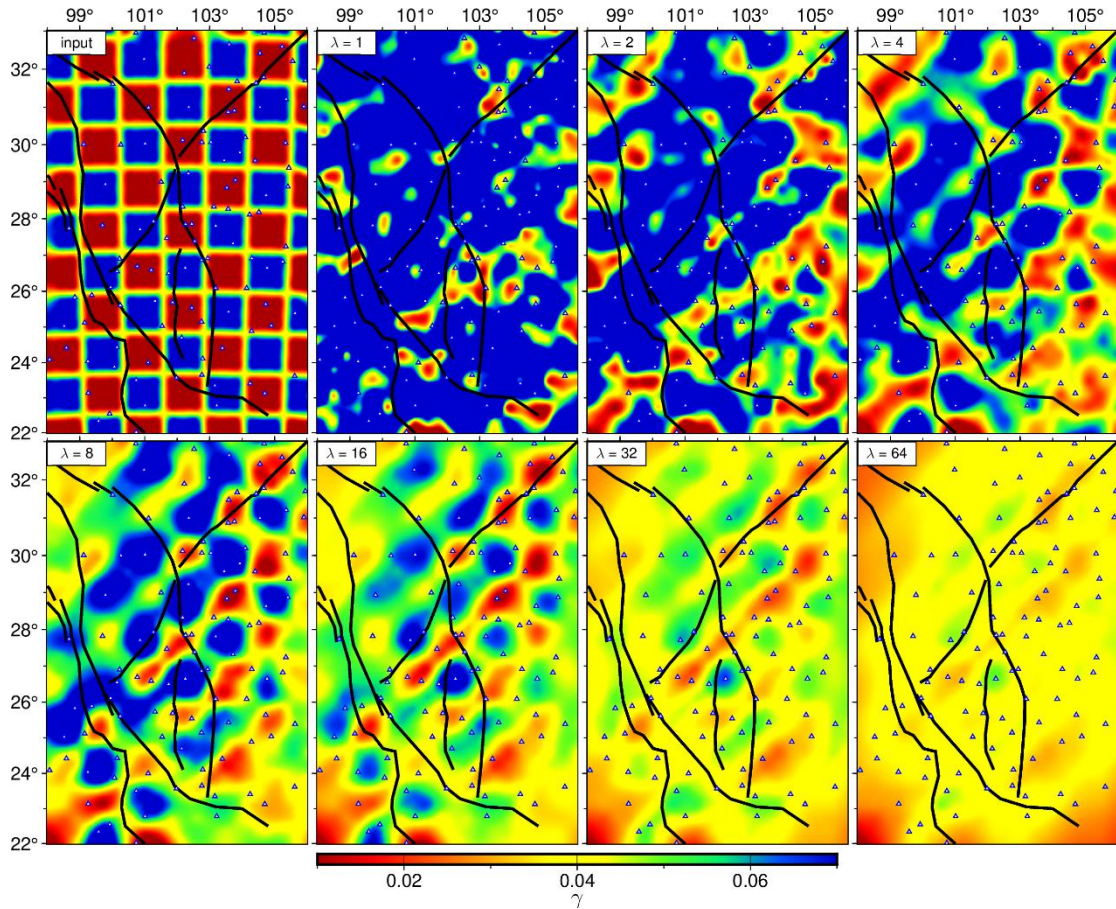
112

113 **Figure S11.** Resolution tests for the azimuth of symmetry axis using  $1^\circ \times 1^\circ$  checkerboard  
 114 with substantially increased standard deviation (0.3 s) of the Gaussian noise. (Top-left) The  
 115 input model has horizontally alternating azimuthal angles of fast axes  $\phi_f = 90^\circ$  and  $\phi_f =$   
 116  $45^\circ$  shown by both the color and the directions of the line segments, and a fixed anisotropy  
 117 strength  $\gamma = 4\%$  represented by the lengths of the line segments. The other panels show  
 118 the recovered models at a depth of 55 km for different damping factors  $\lambda$ .  
 119



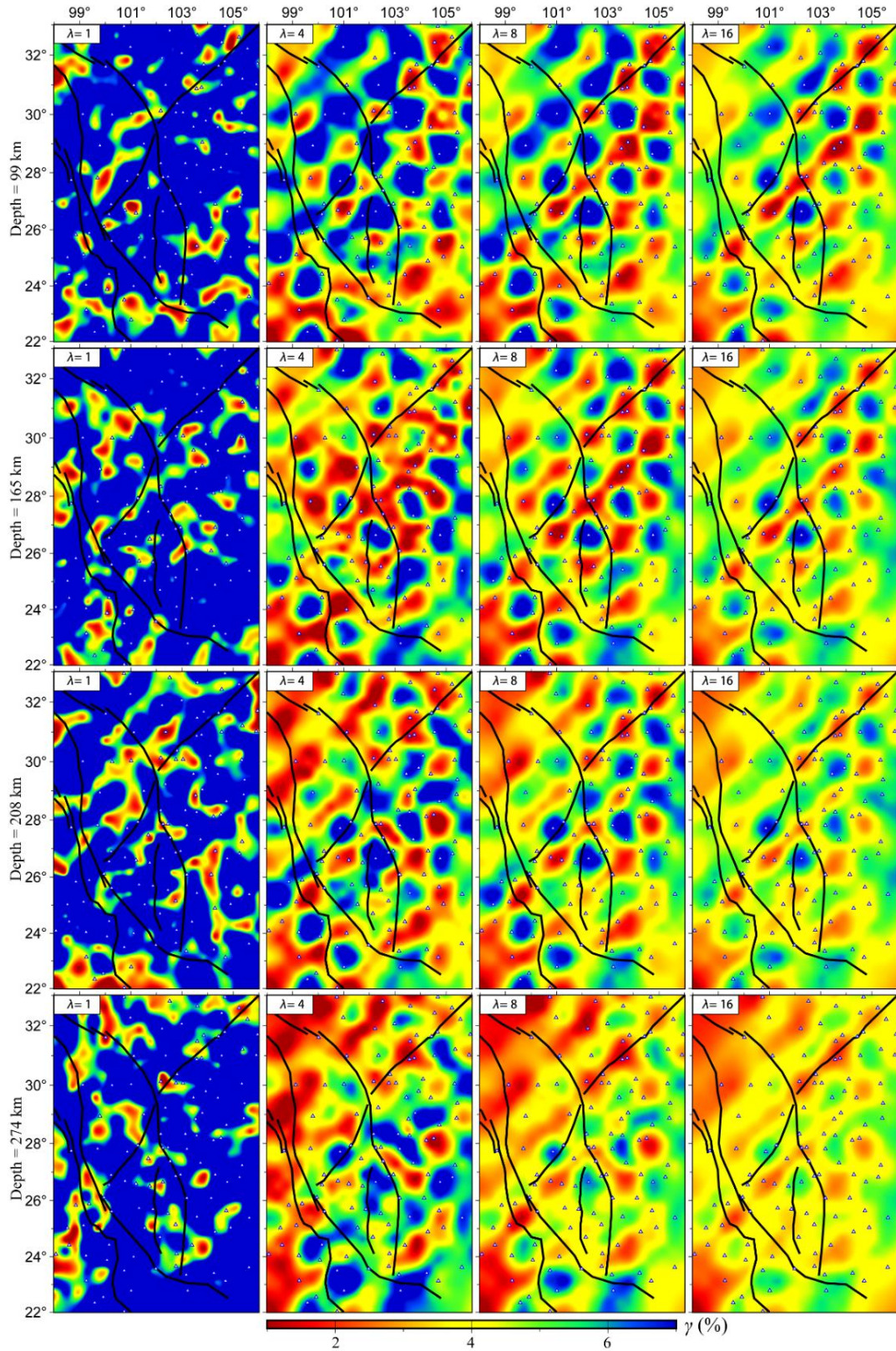
120

121 **Figure S12.** Recovered models for the same resolution test in Figure S11 using for different  
 122 damping factors (left to right) at different depths (top to bottom).



123

124 **Figure S13.** Resolution test for anisotropy strength using  $1^\circ \times 1^\circ$  checkerboard with  
 125 substantially increased standard deviation (0.3 s) of the Gaussian noise. (Top-left) The  
 126 input model has horizontally alternating anisotropy strengths shown by the colors  
 127 representing perturbations of  $\delta\gamma = \pm 3\%$  relative to a background anisotropy strength of  
 128  $\gamma = 4\%$ , and a fixed azimuthal angle of symmetry axis  $\phi_f = 22.5^\circ$ . The other panels show  
 129 the recovered models at a depth of 55 km for different damping factors  $\lambda$ .  
 130



131

132 **Figure S14.** Recovered models for the same resolution test in Figure S13 using for different  
 133 damping factors (left to right) at different depths (top to bottom).